Piano bridge mobility and longitudinal precursors

Guillaume Castera, Juliette Chabassier, Paul Fisette, Brad Wagijo

Piano bridge mobility and longitudinal precursors

Guillaume Castera, Juliette Chabassier, Paul Fisette, Brad Wagijo

RESEARCH REPORT
N° 9530
December 2023
Project-Team MAKUTU

ISSN 0249-6399 ISRN INRIA/RR--9530--FR+ENG

Piano bridge mobility and longitudinal precursors

Guillaume Castera*, Juliette Chabassier*, Paul Fisette†, Brad Wagijo*

Project-Team MAKUTU

Research Report n° 9530 — December 2023 — 46 pages

Abstract: This report is devoted to the modelling of the complex movements of the piano bridge for the transmission of waves between the strings and the soundboard. The model allows accurate transmission of longitudinal waves by taking into account the rotational movements of the bridge and their transmission to the shear directions of the soundboard, modelled as a Reissner-Mindlin plate. The addition of these mobilities, which to our knowledge had never been modelled before in the context of the coupling between a non-linear string and a soundboard, makes it possible to observe longitudinal precursors. We also propose a study of the influence of the angular orientation of the string relative to the soundboard on the power transmitted via the bridge. This study, made possible by our numerical simulation tool, could have applications for instrument making.

Key-words: Piano bridge, Soundboard, Coupling, Numerical simulation, Power balance, String orientation, Transmitted power

* Makutu team, Inria Bordeaux - Sud-Ouest
† iMMC, Université catholique de Louvain, Louvain-La-Neuve, Belgium

RESEARCH CENTRE
BORDEAUX – SUD-OUEST

200 avenue de la Vieille Tour
33405 Talence Cedex

Mobilité du chevalet de piano et précurseurs longitudinaux

Résumé : Ce rapport est consacré à la modélisation des mouvements complexes du chevalet de piano pour la transmission des ondes entre les cordes et la table d'harmonie. Le modèle permet une transmission fidèle des ondes longitudinales par la prise en compte des mouvements de rotation du chevalet et leur transmission aux directions de cisaillement de la table d'harmonie, modélisée comme une plaque de Reissner-Mindlin. L'ajout de ces mobilités, qui à notre connaissance n'avaient jamais été modélisées auparavant dans le contexte du couplage entre une corde non-linéaire et une table d'harmonie, permet d'observer des précurseurs longitudinaux. Nous proposons également une étude de l'influence de l'orientation angulaire de la corde par rapport à la table d'harmonie sur la puissance transmise via le chevalet. Cette étude, rendue possible par notre outil de simulation numérique, pourrait avoir des applications pour la facture instrumentale.

Mots-clés : Chevalet de piano, Table d'harmonie, Couplage, Simulation numérique, Bilan d'énergie, Orientation des cordes, Puissance transmise

Contents

1 Introduction

Although the strings are the elements that produce the sound through their vibrations, a piano, like all stringed instruments, would be inaudible without a soundboard, because the surface area of the strings in contact with the ambient air is too small.
A soundboard is a thin wooden plate that allows the vibrations of the strings to be transmitted to the ambient air with a much larger surface area and therefore much greater power. The choice of wood for soundboards, its growth, cutting, drying, etc, is part of the expertise of the instrument makers and contributes greatly to the sound produced.

To transmit the vibrations from the strings to the soundboard, an element is needed to create an acoustic bridge between them. This is the purpose of the piano bridge.

This is a wooden beam, usually between 20 and 60 millimetres high, glued to the soundboard and over which the strings are attached. Piano makers pay particular attention to the adjustment and construction of the bridge, as it has a considerable influence on the sound [Corradi et al., 2017]. Through years of evolution, it is one of the most complex mechanisms on the piano, as evidenced, for example, by the zig-zag attachments of the strings to its surface.
Although originally made from a single piece of wood, today's bridges are mostly laminated and assembled from wood. This gives greater flexibility in the choice of species, and also reduces the risk of cracking. Some bridges are even drilled to reduce their weight and increase their mobility.

Figure 1: A piano bridge.

The vast majority of modern pianos have two separate bridges for the bass and treble strings. This is the result of a compromise aimed at maximising the length of the strings while keeping their attachment points as far away as possible from the fixed edges of the soundboard for optimum sound rendering. In fact, just as on a drum, a strike close to the fixed edge emits much less sound than a strike centred on it.
To further optimise this point of attachment in relation to the length of the strings, many of today's pianos have a cantilever bass bridge which allows them to be closer to the centre of the soundboard.
Finally, the down bearing, i.e. the load exerted by the strings on the soundboard through the bridge, is certainly one of the most important and sensitive adjustments made by piano makers. For optimum sound transmission, neither too much pressure, which would muffle the vibrations, nor too little pressure, which would transmit too few waves, is required.

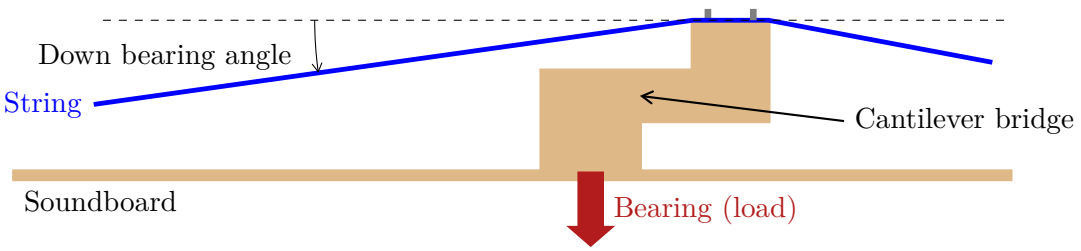

In practice, this bearing is adjusted by setting the angle of the strings from the horizontal, known as the down bearing angle. At zero angle, the string exerts no pressure on the soundboard and transmits very little vibration. The greater the angle, the greater the force exerted on the bridge and the greater the risk of muffling the sound [Reblitz, 2005].

The aim of our study is not to reproduce exactly all the complexities present at this point on the instrument, but to model a mechanical behaviour that can account for the transmission of waves, particularly longitudinal waves.
Experimental studies have been carried out in [Conklin, 1996] and [Giordano, 1998] and identify two possible explanations for the transmission of longitudinal waves via the bridge: the down bearing angle and/or a rotational and torsional movement of the bridge.
Bridge models already exist in the literature and can be used to test some of these hypotheses. For example, [Cuenca and Caussé, 2007] and [Pfeifle, 2014] model the transmission of the transverse wave from a linear Euler-Bernoulli string to a soundboard.
[Valiente et al., 2022] focuses on the different transversal polarizations of a linear Euler-Bernoulli string coupled to a soundboard through a mobility matrix.
The previous models being linear, they do not account for the longitudinal waves. On the contrary, [Tan, 2017] models the interaction of a doubly polarised non-linear string with a bridge that is mobile in all directions in space, but does not allow coupling to a soundboard. [Chabassier, 2012] couples the transverse and longitudinal vibrations of a non-linear string to a bridge movable perpendicular to the soundboard, with a loading angle. The author notes that longitudinal waves are present, but largely underestimated if the angle corresponds to that of a real instrument. To observe correct transmission, the angle must be overestimated and no longer corresponds to a possible configuration on a piano, which implies that another mechanism must allow longitudinal waves to be transmitted.

However, there is currently no model that takes into account the rotational or torsional movements of a bridge coupled to a soundboard, or the effect of these movements on the transmission of longitudinal waves.

In [Podlesak and Lee, 1988], the authors carry out the following experiment. An accelerometer is placed on the bridge to measure its mobility perpendicular to the soundboard, and a microphone is placed in the room to record the sound. They observe that the microphone detects a sound signal even before the accelerometer detects the presence of a wave at the bridge. This confirms that a longitudinal wave, with a faster propagation speed than the transverse wave, propagates in the string and forms a longitudinal precursor. We would like our model to accurately represent the presence of this precursor.

In this report, we present a model of wave transmission between a string and a soundboard modelled as a Reissner-Mindlin vibrating plate [Reissner, 1945], taking into account the main spatial movements of the bridge. In particular, we add to the model presented in [Chabassier, 2012] the rotational movements of the bridge and their coupling with the shear components of the table. The model and its discrete equivalent preserve power balances to ensure the numerical stability of the coupling. Finally, we show that these refinements allow longitudinal waves to be transmitted and longitudinal precursors to be observed with realistic down bearing angles.

2 The soundboard as a Reissner-Mindlin plate

Piano soundboards are quite thin, usually 6 to 10 millimeters thick. Consequently, one of the three dimensions (the thickness) is very small compared with the other two (the length and width), which can measure several meters on large concert pianos. This observation led to consider a reduced model of the equations of 3D linear elastodynamics, and to model the soundboard not as a three-dimensional solid, but as a plate with only two dimensions. Existing plate models include the Kirchoff-Love model, adapted for thin plates and which can be compared to the d'Alembert model for a one-dimensional string, and the Reissner-Mindlin model for thicker and stiffer plates, whose one-dimensional equivalent would be the Timoshenko model.

2.1 The Reissner-Mindlin model

In continuity with the work of [Chabassier, 2012] we use and describe in the following the Reissner-Mindlin model detailed in [Grob, 2006] for which three equations describe a membrane motion of plate elevation u_p and two shear motions described by two angles $\underline{\theta}_p = {}^t(\theta_p^1, \theta_p^2)$ on a bounded domain $\Omega \subset \mathbb{R}^2$.
δ is the plate thickness, ρ the density, E_x and E_y the Young's moduli, G_{xy} G_{xz} and G_{yz} the shear moduli, $\underline{\kappa}$ the shear correction coefficient, $\underline{\nu}$ the Poisson's ratio and ε the linearized strain tensor. Here, z is the direction perpendicular to the plate. We begin here by writing down the boundary conditions for clamped plate, i.e. the Dirichlet conditions.

Model 2.1 (Reissner-Mindlin)

Seek $(u_p, \underline{\theta}_p) : \Omega \times [0,T] \longrightarrow \mathbb{R}^3$ so that

$$(\mathscr{P}) \begin{cases} \rho\delta\, \partial_t^2 u_p - \delta\, \mathrm{div}(\underline{\kappa}^2 \cdot \underline{G} \cdot (\underline{\nabla} u_p + \underline{\theta}_p)) = f & \text{(2.1a)} \\ \rho\dfrac{\delta^3}{12}\, \partial_t^2 \underline{\theta}_p - \dfrac{\delta^3}{12}\underline{\mathrm{Div}}(\mathbb{C}\, \varepsilon(\underline{\theta}_p)) + \delta\, \underline{\kappa}^2 \cdot \underline{G} \cdot (\underline{\nabla} u_p + \underline{\theta}_p) = \underline{\mu} & \text{(2.1b)} \\ u_p = \underline{\theta}_p = 0 \qquad \text{on } \partial\Omega \quad \text{(Clamped)} & \text{(2.1c)} \end{cases}$$

and for all symmetrical strain tensor ε

$$\mathbb{C}\,\varepsilon = \begin{pmatrix} \dfrac{E_x}{1-\nu_{xy}\nu_{yx}} & -\dfrac{E_y\nu_{xy}}{1-\nu_{xy}\nu_{yx}} & 0 \\ -\dfrac{E_x\nu_{yx}}{1-\nu_{xy}\nu_{yx}} & \dfrac{E_y}{1-\nu_{xy}\nu_{yx}} & 0 \\ 0 & 0 & 2G_{xy} \end{pmatrix} \begin{pmatrix} \varepsilon_{xx} \\ \varepsilon_{yy} \\ \varepsilon_{xy} \end{pmatrix}, \quad \underline{G} = \begin{pmatrix} G_{xz} \\ G_{yz} \end{pmatrix}, \quad \underline{\kappa}^2 = \begin{pmatrix} \kappa_x^2 \\ \kappa_y^2 \end{pmatrix}$$

f and $\underline{\mu} = \begin{pmatrix} \mu_1 \\ \mu_2 \end{pmatrix}$ are the source terms of flexion and sheer.

To condense the writings, we rewrite this system in the following matrix form

$$\begin{cases} \mathbb{M}\ddot{\Lambda}_p + \mathbb{R}\Lambda_p = F_p & \text{in } \Omega & \text{(2.2a)} \\ \Lambda_p = 0 & \text{on } \partial\Omega & \text{(2.2b)} \end{cases}$$

where

$$\Lambda_p = \begin{pmatrix} u_p \\ \underline{\theta}_p \end{pmatrix}, \quad \mathbb{M} = \begin{pmatrix} \rho\delta & 0 \\ 0 & \rho\frac{\delta^3}{12} \end{pmatrix}, \quad \mathbb{R} = \begin{pmatrix} \mathcal{B} & \mathcal{C}^* \\ \mathcal{C} & \mathcal{A} \end{pmatrix}, \quad F_p = \begin{pmatrix} f \\ \underline{\mu} \end{pmatrix} \tag{2.3}$$

The operators $\mathcal{A}$, $\mathcal{B}$ and $\mathcal{C}$ are defined as

$$\begin{cases} \mathcal{A}\underline{\theta} = -\dfrac{\delta^3}{12}\underline{\mathrm{Div}}(\mathbb{C}\varepsilon(\underline{\theta})) + \delta\underline{\kappa}^2 \cdot \underline{G} \cdot \underline{\theta} & \text{(2.4a)} \\ \mathcal{B}u = -\delta\ \mathrm{div}(\underline{\kappa}^2 \cdot \underline{G} \cdot \underline{\nabla} u) & \text{(2.4b)} \\ \mathcal{C}u = \delta\ \underline{\kappa}^2 \cdot \underline{G} \cdot \underline{\nabla} u & \text{(2.4c)} \\ \mathcal{C}^*\underline{\theta} = -\delta\ \underline{\kappa}^2 \cdot \underline{G} \cdot \mathrm{div}\ \underline{\theta} & \text{(2.4d)} \end{cases}$$

2.2 Modal decomposition

The $\mathbb{R}$ operator involving second-order derivatives in space is self-adjoint and can therefore be diagonalized.

Let $\mathcal{D}_{\mathbb{R}} = \left\{ \Lambda_p \in \left(H^1(\Omega)\right)^3 \mid \mathbb{R}\Lambda_p \in L^2(\Omega)^3 \right\}$ be the domain of the operator $\mathbb{R}$.

As detailed in [Chabassier, 2012, p. 80], the spectral theorem ensures that there exists an orthonormal sequence $(w_n)_{n\in\mathbb{N}^*}$ of elements of $\mathcal{D}_{\mathbb{R}}$ which forms a Hilbertian basis of $\left(L^2(\Omega)\right)^3$ and a sequence $(\lambda_n)_{n\in\mathbb{N}^*}$ of positive real numbers which tends to $+\infty$ such that

$$\forall n \in \mathbb{N}^*, \quad \mathbb{R}w_n = \lambda_n \mathbb{M} w_n \tag{2.5}$$

The solution Λ_p and the source term F can then be decomposed in the basis $(w_n)_{n\in\mathbb{N}^*}$

$$\forall (x,y,t) \in \Omega \times \mathbb{R}_+, \quad \begin{cases} \Lambda_p(x,y,t) = \displaystyle\sum_{n\in\mathbb{N}^*} \Lambda_{p,n}(t) w_n(x,y) & \text{(2.6a)} \\ F_p(x,y,t) = \displaystyle\sum_{n\in\mathbb{N}^*} F_{p,n}(t) w_n(x,y) & \text{(2.6b)} \end{cases}$$

which allows us to rewrite the Reissner-Mindlin equations as a system of decoupled ordinary differential equations (ODEs) verified by the modal amplitudes

$$\forall n \in \mathbb{N}^*, \quad \ddot{\Lambda}_{p,n} + \lambda_n \Lambda_{p,n} = F_{p,n} \tag{2.7}$$

This description already shows the numerical interest of modal decomposition by using a truncated system of N_m modes, and the method of resolution will consist of determining the N_m modal amplitudes of the solution at each simulation time step.

We refer to [Chabassier, 2012, p. 82] for detailed explanations of the damping phenomena that take place in the soundboard. Just note that we use a modal damping model intrinsic to each mode, for which each frequency is attenuated differently according to an experimental model based on measurements by [Ege, 2009] and [Bucur, 2006]. It takes the form $f_{ve}(\lambda) = a\lambda + b\sqrt{\lambda} + c$ and allows us to rewrite the equations (2.7) with a viscoelastic damping factor

$$\forall n \in \mathbb{N}^*, \quad \ddot{\Lambda}_{p,n} + f_{ve}(\lambda_n)\dot{\Lambda}_{p,n} + \lambda_n \Lambda_{p,n} = F_{p,n} \tag{2.8}$$

More generally, a linear operator $f_{ve}(\mathbb{R})$ can be defined such that for any eigenmode w_n, $f_{ve}(\mathbb{R})w_n = f_{ve}(\lambda_n)\mathbb{M}w_n$.

This gives a damped matrix formulation of the Reissner-Mindlin system:

Model 2.2 (Abstract damped Reissner-Mindlin formulation)

Seek $\Lambda_p : \Omega \times [0,T] \longrightarrow \mathbb{R}^3$ so that

$$\begin{cases} \mathbb{M}\ddot{\Lambda}_p + f_{ve}(\mathbb{R})\dot{\Lambda}_p + \mathbb{R}\Lambda_p = F_p & \text{in } \Omega \quad (2.9a) \\ \Lambda_p = 0 & \text{on } \partial\Omega \quad (2.9b) \end{cases}$$

2.3 Variational formulation and energy

Let us introduce the variational space

$$\mathcal{L}_D = \left\{ \Lambda_p \in \left(H^1(\Omega)\right)^3 \;\middle|\; \forall k \in \mathcal{J}_D,\ (\Lambda_p)_k = 0 \quad \text{on } \partial\Omega \right\}$$

The set $\mathcal{J}_D$ is used to specify which components are subject to Dirichlet conditions. For clamped edge conditions, $\mathcal{J}_D = \{1,2,3\}$ and the space is simply $\mathcal{L}_D = \left(H_0^1(\Omega)\right)^3$. For the simply supported conditions we'll use for simulations, $\mathcal{J}_D = \{1\}$ which allows us to impose the Dirichlet condition only on the u_p elevation motion, the other components being subject to Neumann conditions.

Seek $\Lambda_p \in \mathcal{L}_D$ so that for all $\Lambda_p^* \in \mathcal{L}_D$

$$\int_\Omega \mathbb{M}\ddot{\Lambda}_p \cdot \Lambda_p^* + \int_\Omega f_{ve}(\mathbb{R})\dot{\Lambda}_p \cdot \Lambda_p^* + \int_\Omega \mathbb{R}\Lambda_p \cdot \Lambda_p^* = \int_\Omega F_p \cdot \Lambda_p^* \tag{2.10}$$

In accordance with the previous paragraph, all modes $(\lambda_n, w_n)_{n\in\mathbb{N}^*}$ satisfy at the variational level

$$\forall n \in \mathbb{N}^*, \quad \forall \Lambda_p^* \in \mathcal{L}_D, \quad \int_\Omega \mathbb{R}w_n \cdot \Lambda_p^* = \lambda_n \int_\Omega \mathbb{M}w_n \cdot \Lambda_p^* \tag{2.11}$$

Theorem 2.1 (Power balance of the damped Reissner-Mindlin system)

Any regular enough solution $\Lambda_p \in \mathscr{C}^1([0,T],\mathcal{L}_D) \cap \mathscr{C}^2\left([0,T], L^2([0,L])^3\right)$ to the damped Reissner-Mindlin model 2.2 verifies

$$\begin{cases} \dfrac{d\mathcal{E}_p}{dt} = \displaystyle\int_\Omega F_p \cdot \dot{\Lambda}_p - \left\|\dot{\Lambda}_p\right\|^2_{f_{ve}(\mathbb{R})} & (2.12a) \\ \mathcal{E}_p(t) = \dfrac{1}{2}\left\|\dot{\Lambda}_p\right\|^2_{\mathbb{M}} + \dfrac{1}{2}\left\|\Lambda_p\right\|^2_{\mathbb{R}} & (2.12b) \end{cases}$$

Proof. We use $\Lambda_p^* = \dot{\Lambda}_p \in \mathcal{L}_D$ in the variational formulation (2.10), and the result follows directly from this. The existence of a solution $\Lambda_p \in \mathscr{C}^1([0,T],\mathcal{L}_D) \cap \mathscr{C}^2\left([0,T], L^2(\Omega)^3\right)$ follows from the application of the Hille-Yosida theorem to the Reissner-Mindlin system. The full proof is given in [Grob, 2006]. □

3 Bridge model with rotation mobilities

In [Chabassier, 2012], the choice was made to model only the vertical movement of the bridge (direction $\vec{\nu}$) with a downbearing angle α.
Simulation results show, however, that longitudinal modes are greatly under-represented in the sound produced by such a model.

We therefore propose a model that makes the bridge mobile around its point of contact C with the table. At this point, the moments of the forces exerted by the strings are transmitted to the shear directions θ_p^1 and θ_p^2 of the Reissner-Mindlin model. Indeed, the red bridge in figure 2, which has a height ℓ typically between 38 and 64 millimeters, acts as a lever for these forces. For our modelling purposes, we assume that the bridge has no deformation, and therefore no energy, nor does it dissipate any. It is simply seen as a rigid body that acts as a coupling condition between the string and the soundboard.

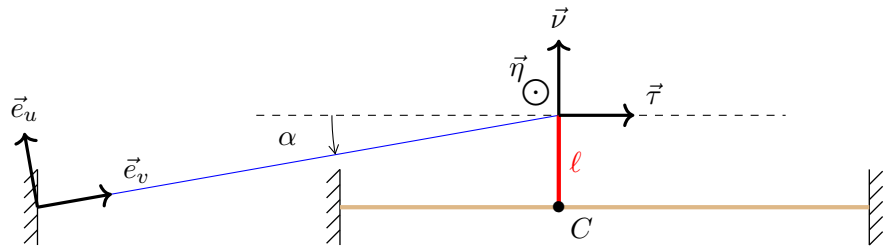

(a) Side view

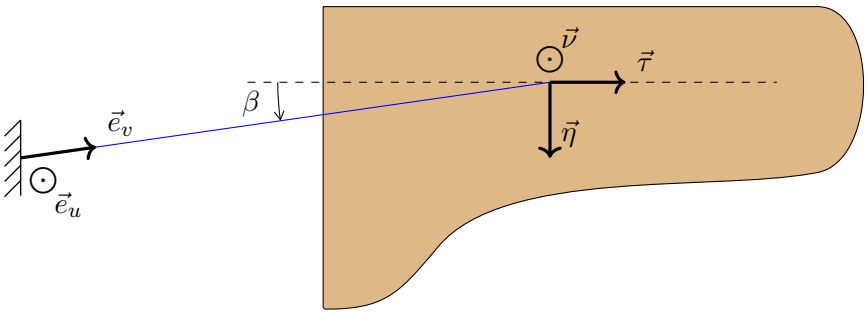

(b) Top view

Figure 2: Diagram of string - bridge - soundboard coupling

The reference frame $(\vec{\eta}, \vec{\tau}, \vec{\nu})$ is a Cartesian frame associated with the soundboard. Consequently, a displacement imposed on the bridge in the $\vec{\tau}$ direction is transmitted purely to the θ_1 shear angle, while a displacement on $\vec{\eta}$ is transmitted purely to θ_2.
We therefore add a lateral angle β to take into account any mismatch between the direction of the strings and the preferred directions of the wood defined by the stress tensor $\mathbb{C}$ of the model 2.1 and the presence of stiffeners.

These two angles α and β, which orient the string relatively to the soundboard plane, are such that

$$\begin{pmatrix} \vec{\nu} \\ \vec{\tau} \\ \vec{\eta} \end{pmatrix} = \begin{pmatrix} \cos(\alpha) & \sin(\alpha) \\ -\sin(\alpha)\cos(\beta) & \cos(\alpha)\cos(\beta) \\ \sin(\alpha)\sin(\beta) & -\cos(\alpha)\sin(\beta) \end{pmatrix} \begin{pmatrix} \vec{e}_u \\ \vec{e}_v \end{pmatrix} \tag{3.1}$$

3.1 Expression of the coupling forces

Let us now denote F^P, G^P and H^P the projections of the force exerted by the strings on the bridge in the three spatial directions $(\vec{\nu}, \vec{\tau}, \vec{\eta})$.
They are taken into account in the right-hand-side of the Reissner-Mindlin equations (2.2) and distributed over the table by a distribution function χ_Ω:

$$\mathbb{M}\ddot{\Lambda}_p + f_{ve}(\mathbb{R})\dot{\Lambda}_p + \mathbb{R}\Lambda_p = F_p = \begin{pmatrix} -F^P(t)\chi_\Omega(x,y) \\ -\ell G^P(t)\chi_\Omega(x,y) \\ -\ell H^P(t)\chi_\Omega(x,y) \end{pmatrix} \tag{3.2}$$

To guarantee stable couplings, we impose an exact conservation of energy: the work transmitted by the strings must be equal to that injected into the soundboard. Thanks to the theorems A.1 and 2.1, it writes

$$T_L \cdot \dot{q}(x = L, t) + \int_\Omega F_p \cdot \dot{\Lambda}_p = 0 \tag{3.3}$$

with $T_L = \Big[A\partial_x q + Bq + \nabla\mathcal{U}(\partial_x q) + H\partial_x \dot{q}\Big](x = L, t)$

This is achieved by imposing continuity of the speeds at the bridge:

$$\begin{cases} \dot{q}(L,t) \cdot \nu_c = \displaystyle\int_\Omega \dot{u}_p \chi_\Omega & \text{(3.4a)} \\ \dot{q}(L,t) \cdot \tau_c = \ell \displaystyle\int_\Omega \dot{\theta}^1_p \chi_\Omega & \text{(3.4b)} \\ \dot{q}(L,t) \cdot \eta_c = \ell \displaystyle\int_\Omega \dot{\theta}^2_p \chi_\Omega & \text{(3.4c)} \end{cases}$$

where ν_c, τ_c and η_c are the vectors used to select those components of the string unknown that have physical positional significance. For example, for the Timoshenko system, we have

$$\dot{q}(L,t) \cdot \nu_c = \begin{pmatrix} \dot{u}_c(L,t) \\ 0 \\ 0 \end{pmatrix} \cdot \vec{\nu} \tag{3.5}$$

The physically dimensionless shear component φ_c, which is not involved in calculating the end-point velocity, has no projection in this base. For the geometrically exact model we have

$$\dot{q}(L,t) \cdot \nu_c = \begin{pmatrix} \dot{u}_c(L,t) \\ \dot{v}_c(L,t) \\ 0 \end{pmatrix} \cdot \vec{\nu} \tag{3.6}$$

The energy conservation equation (3.3) can then be rewritten as follows

$$\begin{aligned} T_L \cdot \dot{q}(L,t) &= -\int_\Omega F_p \cdot \dot{\Lambda}_p & \text{(3.7)} \\ &= F^P(t) \int_\Omega \dot{u}_p \chi_\Omega + \ell G^P(t) \int_\Omega \dot{\theta}^1_p \chi_\Omega + \ell H^P(t) \int_\Omega \dot{\theta}^2_p \chi_\Omega & \text{(3.8)} \\ &= \left[\dot{q}(L,t) \cdot \nu_c\right] F^P(t) + \left[\dot{q}(L,t) \cdot \tau_c\right] G^P(t) + \left[\dot{q}(L,t) \cdot \eta_c\right] H^P(t) & \text{(3.9)} \end{aligned}$$

By identification, the expression of the coupling forces are obtained

$$\begin{cases} F^P(t) = T_L \cdot \nu_c & \text{(3.10a)} \\ G^P(t) = T_L \cdot \tau_c & \text{(3.10b)} \\ H^P(t) = T_L \cdot \eta_c & \text{(3.10c)} \end{cases}$$

Model 3.1 (String - Soundboard coupling)

Seek $q : [0, L] \times [0, T] \longrightarrow \mathbb{R}^N$, $\Lambda_p : \Omega \times [0, T] \longrightarrow \mathbb{R}^3$ so that

String equation:

$$\partial_t^2 Mq + \partial_t(Rq - \partial_x(H\partial_x q)) - \partial_x(A\partial_x q + Bq + \nabla\mathcal{U}(\partial_x q)) + Cq + {}^tB\partial_x q = F(x,t) \tag{3.11a}$$

Boundary conditions for the string:

$$\begin{cases} \forall k \in \mathcal{I}_D, & q_k(0,t) = 0 \\ \forall k \in \mathcal{I}_N, & \partial_x q_k(0,t) = 0 \end{cases} \quad \text{and} \quad \begin{cases} \dot{q}(L,t)\cdot\tau_c = \displaystyle\int_\Omega \dot{u}_p\chi_\Omega \\ \dot{q}(L,t)\cdot\nu_c = \ell\displaystyle\int_\Omega \dot{\theta}_p^1\chi_\Omega \\ \dot{q}(L,t)\cdot\eta_c = \ell\displaystyle\int_\Omega \dot{\theta}_p^2\chi_\Omega \end{cases} \tag{3.11b}$$

Coupling forces exerted on the soundboard :

$$\begin{cases} F^P(t) = T_L\cdot\nu_c \\ G^P(t) = T_L\cdot\tau_c \\ H^P(t) = T_L\cdot\eta_c \end{cases} \quad \text{où} \quad T_L = \left[A\partial_x q + Bq + \nabla\mathcal{U}(\partial_x q) + H\partial_x\dot{q}\right](L,t) \tag{3.11c}$$

Soundboard equation:

$$\mathbb{M}\ddot{\Lambda}_p + f_{ve}(\mathbb{R})\dot{\Lambda}_p + \mathbb{R}\Lambda_p = F_p = \begin{pmatrix} -F^P(t)\chi_\Omega(x,y) \\ -\ell G^P(t)\chi_\Omega(x,y) \\ -\ell H^P(t)\chi_\Omega(x,y) \end{pmatrix} \quad \text{in } \Omega \tag{3.11d}$$

Boundary conditions for the soundboard:

$$\forall k \in \mathcal{J}_D,\ (\Lambda_p)_k = 0 \quad \text{on } \partial\Omega \tag{3.11e}$$

This model now allows bridge mobility in the ν_c and η_c directions, which was not the case in the work of [Chabassier, 2012]. It also allows coupling to a soundboard, which was not the case in [Tan, 2017]. The coupling is achieved by imposing a continuity of velocities between the end of the string attached to the bridge and the soundboard, which also ensures conservation of energy.

3.2 Variational formulation and energy

Let us introduce the variational spaces involved

$$\mathcal{Q}_D = \left\{ q \in \left(H^1([0,L])\right)^N \;\middle|\; \forall k \in \mathcal{I}_D,\ q_k(0) = 0 \right\} \qquad \text{for the string}$$

$$\mathcal{L}_D = \left\{ \Lambda_p \in \left(H^1(\Omega)\right)^3 \;\middle|\; \forall k \in \mathcal{J}_D,\ (\Lambda_p)_k = 0 \quad \text{on } \partial\Omega \right\} \qquad \text{for the soundboard}$$

Seek $q : [0,T] \longrightarrow \mathcal{Q}_D$, $\Lambda_p : [0,T] \longrightarrow \mathcal{L}_D$ and $F^P, G^P, H^P : [0,T] \longrightarrow \mathbb{R}$ so that for all $(q^*, \Lambda_p^*) \in \mathcal{Q}_D \times \mathcal{L}_D$:

$$
\begin{cases}
\text{String equation:} \\
\displaystyle\int_0^L M\ddot{q}\cdot q^* + \int_0^L R\dot{q}\cdot q^* + \int_0^L H\partial_x\dot{q}\cdot\partial_x q^* + \int_0^L \begin{pmatrix} C & {}^tB \\ B & A \end{pmatrix}\begin{pmatrix} q \\ \partial_x q \end{pmatrix}\cdot\begin{pmatrix} q^* \\ \partial_x q^* \end{pmatrix} \\
\qquad + \displaystyle\int_0^L \nabla\mathcal{U}(\partial_x q)\cdot\partial_x q^* = \int_0^L F\cdot q^* \\
\qquad\qquad + F^P(t)\Big[q^*(L,t)\cdot\nu_c\Big] + G^P(t)\Big[q^*(L,t)\cdot\tau_c\Big] + H^P(t)\Big[q^*(L,t)\cdot\eta_c\Big]
\end{cases} \tag{3.12a}
$$

$$
\begin{cases}
\text{Coupling equations:} \\
\begin{cases}
\dot{q}(L,t)\cdot\nu_c = \displaystyle\int_\Omega \dot{u}_p\chi_\Omega \\
\dot{q}(L,t)\cdot\tau_c = \ell\displaystyle\int_\Omega \dot{\theta}_p^1\chi_\Omega \\
\dot{q}(L,t)\cdot\eta_c = \ell\displaystyle\int_\Omega \dot{\theta}_p^2\chi_\Omega
\end{cases}
\end{cases} \tag{3.12b}
$$

$$
\begin{cases}
\text{Soundboard equation:} \\
\displaystyle\int_\Omega \mathbb{M}\ddot{\Lambda}_p\cdot\Lambda_p^* + \int_\Omega f_{ve}(\mathbb{R})\dot{\Lambda}_p\cdot\Lambda_p^* + \int_\Omega \mathbb{R}\Lambda_p\cdot\Lambda_p^* = \\
\qquad - F^P(t)\displaystyle\int_\Omega u_p^*\chi_\Omega - G^P(t)\ell\int_\Omega \theta_p^{1*}\chi_\Omega - H^P(t)\ell\int_\Omega \theta_p^{2*}\chi_\Omega
\end{cases} \tag{3.12c}
$$

The forces F^P, G^P and H^P are Lagrange multipliers associated with coupling constraints in the three directions of space.

Remark 3.1

Consider a string simply polarized in the vertical direction $\vec{e}_u$. If $\beta \equiv 0[\pi]$, there is no projection of motion in the $\vec{\eta}$ direction and the third coupling equation in the η_c direction boils down to $0 = 0$, leading to an ill-posed system. To overcome this problem, the multiplier H^P and the associated coupling equation on η_c are eliminated for simulations in which $\beta \equiv 0\,[\pi]$.

Theorem 3.1 (Power balance of the string - soundboard system)

Any regular enough solution $q \in \mathscr{C}^1([0,T],\mathcal{Q}_D)\cap\mathscr{C}^2\left([0,T],L^2([0,L])^N\right)$ and $\Lambda_p \in \mathscr{C}^1([0,T],\mathcal{L}_D)\cap\mathscr{C}^2\left([0,T],L^2(\Omega)^3\right)$ to the model 3.1 verifies

$$
\begin{cases}
\dfrac{d\mathcal{E}_{c,p}}{dt} = \displaystyle\int_0^L F\cdot\dot{q} - \int_0^L R\dot{q}\cdot\dot{q} - \int_0^L H\partial_x\dot{q}\cdot\partial_x\dot{q} - \left\|\dot{\Lambda}_p\right\|^2_{f_{ve}(\mathbb{R})} & \text{(3.13a)} \\
\mathcal{E}_{c,p}(t) = \mathcal{E}_c(t) + \mathcal{E}_p(t) & \text{(3.13b)}
\end{cases}
$$

where $\mathcal{E}_c$ is the energy of the string defined by theorem A.1 and $\mathcal{E}_p$ is the energy of the soundboard defined by theorem 2.1.

Proof. The power balance of the string A.1 ensures that

$$\frac{d\mathcal{E}_c}{dt} = T_L \cdot \dot{q}(L,t) + \int_0^L F \cdot \dot{q} - \int_0^L R\dot{q} \cdot \dot{q} - \int_0^L H\partial_x \dot{q} \cdot \partial_x \dot{q} \tag{3.14}$$

and that of the soundboard 2.1 that

$$\begin{aligned} \frac{d\mathcal{E}_p}{dt} &= \int_\Omega F_p \cdot \dot{\Lambda}_p - \left\|\dot{\Lambda}_p\right\|^2_{f_{ve}(\mathbb{R})} && (3.15)\\ &= -F^P(t)\int_\Omega \dot{u}_p\chi_\Omega - G^P(t)\ell\int_\Omega \dot{\theta}^1_p\chi_\Omega - H^P(t)\ell\int_\Omega \dot{\theta}^2_p\chi_\Omega - \left\|\dot{\Lambda}_p\right\|^2_{f_{ve}(\mathbb{R})} && (3.16)\end{aligned}$$

According to the definitions of coupling forces (3.11d) we have

$$T_L \cdot \dot{q}(L,t) = F^P(t)\Big[\dot{q}(L,t)\cdot\nu_c\Big] + G^P(t)\Big[\dot{q}(L,t)\cdot\tau_c\Big] + H^P(t)\Big[\dot{q}(L,t)\cdot\eta_c\Big] \tag{3.17}$$

then the coupling conditions (3.12b) allow to write that

$$T_L \cdot \dot{q}(L,t) = F^P(t)\int_\Omega \dot{u}_p\chi_\Omega + G^P(t)\ell\int_\Omega \dot{\theta}^1_p\chi_\Omega + H^P(t)\ell\int_\Omega \dot{\theta}^2_p\chi_\Omega \tag{3.18}$$

The sum of the two power balances concludes the demonstration. By construction, all coupling terms vanish to guarantee a coupling that transfers energy exactly between the two subsystems. □

3.3 Choice of distribution function χ_Ω

The χ_Ω distribution function is used to distribute the force exerted by the string on the soundboard, and thus to convert a point force into a surface force. Several choices are possible, but all must verify that the integral of χ_Ω is 1 over $\mathbb{R}^2$, in order to achieve a weighted average.

In [Chabassier, 2012], χ_Ω is a Gaussian function defined by

$$\forall (x,y) \in \Omega, \quad \chi_\Omega(x,y) = \frac{\gamma}{\pi r_0^2} e^{-\gamma\left(\frac{r}{r_0}\right)^2} \qquad \text{where} \qquad r = \left\| \begin{pmatrix} x - x_0 \\ y - y_0 \end{pmatrix} \right\|_2 \tag{3.19}$$

where γ is a rate of decay, (x_0, y_0) the center of the distribution, and r_0 the radius at which the influence becomes negligible.
This choice is not, however, the most physically suitable for modelling a bridge, which is not very deformable, as the decay of the Gaussian is rather slow and doesn't allow the distribution zone to be focused precisely.

To overcome this shortcoming, we use another normalized distribution function, but one whose decay slope can be adjusted much more precisely

$$\forall (x,y) \in \Omega, \quad \begin{cases} \begin{pmatrix} \tilde{x} \\ \tilde{y} \end{pmatrix} = \begin{pmatrix} \cos\beta_\chi & -\sin\beta_\chi \\ \sin\beta_\chi & \cos\beta_\chi \end{pmatrix} \begin{pmatrix} x \\ y \end{pmatrix} & \text{(3.20a)} \\ \delta_{r,s}(x) = \dfrac{1}{2r}\left(\dfrac{1}{1+e^{-s(x+r)}} - \dfrac{1}{1+e^{-s(x-r)}} \right) & \text{(3.20b)} \\ \chi_\Omega(x,y) = \delta_{r_x,s_x}(\tilde{x})\delta_{r_y,s_y}(\tilde{y}) & \text{(3.20c)} \end{cases}$$

The parameters s_x and s_y are used to adjust the decay rates in the two directions to model the bridge's non-symmetry, and to orient it on the soundboard at an angle β_χ. In the bridge's width, the decay is very fast, and much slower in its length.

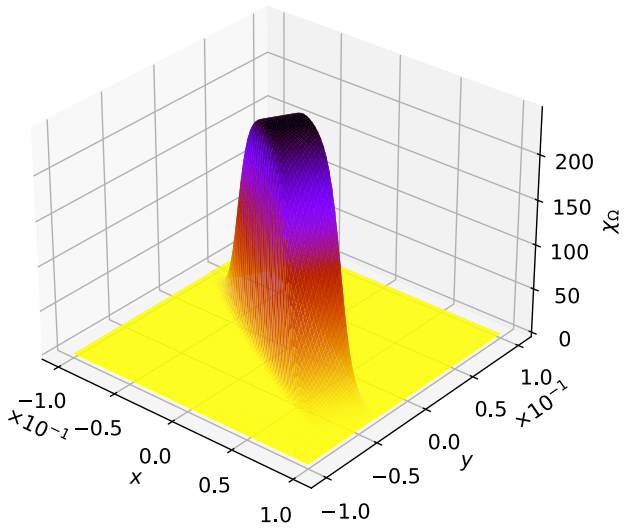

r_x [m]	r_y [m]	s_x [-]	s_y [-]
0,02	0,05	1000	100

x_0 [m]	y_0 [m]	β_χ [°]
0	0	60

Figure 3: Distribution function χ_Ω.

4 Discretization of the coupled string - soundboard model

The discretization techniques used in this section are taken from [Derveaux, 2002] and [Chabassier, 2012]. They have been adapted to take the bridge rotation mobilities into account.

4.1 Numerical scheme for the soundboard

4.1.a Space discretization - Modal method

Let us consider Ω_h a conformal quadrangular mesh of Ω and note

$$\mathcal{L}_h = \left\{ \Lambda_h \in \mathcal{L}_D \;\middle|\; \forall K \in \Omega_h,\ \Lambda_{h|K} \in \mathbb{Q}_r[X,Y]^3 \right\}$$

where $\mathbb{Q}_r[X,Y]$ is the space of polynomials generated by $\{X^i Y^j \mid 1 \leqslant i,j \leqslant r\}$.
In order to make the mass matrix diagonal, Gauss-Lobatto points are used to position the n_h^Λ degrees of freedom of the finite element method, as well as the quadrature points to evaluate the integral terms. The basis functions $(\phi_i)_{i\in[\![1,n_h^\Lambda]\!]}$ are such that for any vertex S_j, $\phi_i(S_j) = \delta_{ij}$.

The modal problem (2.11) can then be written in discrete form:
For all $n \in \mathbb{N}^*$, seek $w_{h,n} \in \mathcal{L}_h$ and $\lambda_{h,n} \in \mathbb{R}$ so that for all $\Lambda_h^* \in \mathcal{L}_h$:

$$\int_\Omega \mathbb{R} w_{h,n} \cdot \Lambda_h^* = \lambda_{h,n} \int_\Omega \mathbb{M} w_{h,n} \cdot \Lambda_h^* \tag{4.1}$$

Evaluating this variational formulation for all basis functions allows us to rewrite this problem in matrix form

$$\mathbb{R}_h W_{h,n} = \lambda_{h,n} \mathbb{M}_h W_{h,n} \tag{4.2}$$

where $W_{h,n}$ is the vector of components of $w_{h,n}$ in the finite element basis. Since the $\mathbb{R}_h$ and $\mathbb{M}_h$ matrices are symmetrical and diagonal positive-definite respectively, the $\mathbb{R}_h$ matrix is diagonalizable in a $\mathbb{M}_h$-orthogonal basis by the spectral theorem. If we denote $\mathbb{P}_h$ the transition matrix from the finite element basis to this new modal basis $(W_{h,n})_{n\in\mathbb{N}^*}$ we have

$$\begin{cases} {}^t\mathbb{P}_h \mathbb{R}_h \mathbb{P}_h = \mathbb{D}_h = \operatorname{diag}(\lambda_{h,n}) \\ {}^t\mathbb{P}_h f_{ve}(\mathbb{R}_h) \mathbb{P}_h = \mathbb{A}_h = \operatorname{diag}(f_{ve}(\lambda_{h,n})) \\ {}^t\mathbb{P}_h \mathbb{M}_h \mathbb{P}_h = \mathbb{I} \end{cases}$$

and any $\Lambda_h \in \mathcal{L}_h$ element can be expressed in the finite element basis Λ_h^{EF} or in the modal basis Λ_h^{mod} by the transformations

$$\begin{cases} \Lambda_h^{EF} = \mathbb{P}_h \Lambda_h^{mod} \\ \Lambda_h^{mod} = {}^t\mathbb{P}_h \mathbb{M}_h \Lambda_h^{EF} \end{cases}$$

The variational formulation of the damped Reissner-Mindlin model (2.10) can then be written in matrix form

$$\mathbb{M}_h \ddot{\Lambda}_h^{EF} + f_{ve}(\mathbb{R}_h) \dot{\Lambda}_h^{EF} + \mathbb{R}_h \Lambda_h^{EF} = F_h \tag{4.5}$$

and then in the modal basis

$$\ddot{\Lambda}_h^{mod} + \mathbb{A}_h \dot{\Lambda}_h^{mod} + \mathbb{D}_h \Lambda_h^{mod} = {}^t\mathbb{P}_h F_h \tag{4.6}$$

The modal resolution method then consists in truncating the sequence of modes to retain only the first N_m, thus considerably reducing the calculation time compared with the number of degrees of freedom of the finite element basis. At the same time, very high-frequency finite element modes, which are polluted by discretization errors anyway, are eliminated [Durufle, 2006].

4.1.b Analytical resolution scheme in time

The time scheme we use consists in considering the second member constant from one time step to the next, which is a legitimate approximation since it is itself derived from a discretization of the strings and therefore no longer depends continuously on time.

Then let us consider that $F_h(t) = F_h(t^n) = F_h^n$ for all $t \in [t^{n-1/2}, t^{n+1/2}]$.

Numerical scheme 4.1 (Scheme for the soundboard)

At each and every iteration, seek $\Lambda_h^{mod,n+1/2} = \Lambda_h^{mod}(t^{n+1/2}) \in \mathbb{R}^{n_h^\Lambda}$ so that

$$\begin{cases} \forall t \in [t^{n-1/2}, t^{n+1/2}], \quad \ddot{\Lambda}_h^{mod}(t) + \mathbb{A}_h \dot{\Lambda}_h^{mod}(t) + \mathbb{D}_h \Lambda_h^{mod}(t) = {}^t\mathbb{P}_h F_h^n & \text{(4.7a)} \\ \Lambda_h^{mod}(t^{n-1/2}) = \Lambda_h^{mod,n-1/2}, \quad \dot{\Lambda}_h^{mod}(t^{n-1/2}) = \dot{\Lambda}_h^{mod,n-1/2} & \text{(4.7b)} \end{cases}$$

It is in fact a system of decoupled ordinary differential equations whose solution at time $t^{n+1/2}$ is given analytically (see appendix C) by

$$\begin{cases} \Lambda_h^{mod,n+1/2} = \Lambda_h^{mod}(t^{n+1/2}) = \mathcal{S}_{\Delta t}^0 \Lambda_h^{mod}(t^{n-1/2}) + \mathcal{S}_{\Delta t}^1 \dot{\Lambda}_h^{mod}(t^{n-1/2}) + \mathcal{R}_{\Delta t}\, {}^t\mathbb{P}_h F_h^n & \text{(4.8a)} \\ \dot{\Lambda}_h^{mod,n+1/2} = \dot{\Lambda}_h^{mod}(t^{n+1/2}) = \dot{\mathcal{S}}_{\Delta t}^0 \Lambda_h^{mod}(t^{n-1/2}) + \dot{\mathcal{S}}_{\Delta t}^1 \dot{\Lambda}_h^{mod}(t^{n-1/2}) + \dot{\mathcal{R}}_{\Delta t}\, {}^t\mathbb{P}_h F_h^n & \text{(4.8b)} \end{cases}$$

Theorem 4.1 (Discrete power balance of the soundboard modal system)

The solution to the scheme 4.1 verifies

$$\begin{cases} \dfrac{\mathcal{E}_p^{n+1/2} - \mathcal{E}_p^{n-1/2}}{\Delta t} = {}^t\mathbb{P}_h F_h^n \cdot \dfrac{\Lambda_h^{mod,n+1/2} - \Lambda_h^{mod,n-1/2}}{\Delta t} - \dfrac{1}{\Delta t} \displaystyle\int_{t^{n-1/2}}^{t^{n+1/2}} \left\| \dot{\Lambda}_h^{mod} \right\|_{\mathbb{A}_h}^2 & \text{(4.9a)} \\ \mathcal{E}_p^{n+1/2} = \dfrac{1}{2} \left\| \dot{\Lambda}_h^{mod,n+1/2} \right\|_2^2 + \dfrac{1}{2} \left\| \Lambda_h^{mod,n+1/2} \right\|_{\mathbb{D}_h}^2 & \text{(4.9b)} \end{cases}$$

Proof. Take the scalar product of equation (4.7a) with $\dot{\Lambda}_h^{mod}(t)$ and integrate for $t \in [t^{n-1/2}, t^{n+1/2}]$:

$$\int_{t^{n-1/2}}^{t^{n+1/2}} \ddot{\Lambda}_h^{mod} \cdot \dot{\Lambda}_h^{mod} + \int_{t^{n-1/2}}^{t^{n+1/2}} \mathbb{D}_h \Lambda_h^{mod} \cdot \dot{\Lambda}_h^{mod} = \int_{t^{n-1/2}}^{t^{n+1/2}} {}^t\mathbb{P}_h F_h^n \cdot \dot{\Lambda}_h^{mod} - \int_{t^{n-1/2}}^{t^{n+1/2}} \mathbb{A}_h \dot{\Lambda}_h^{mod} \cdot \dot{\Lambda}_h^{mod} \quad (4.10)$$

After integration, and since F_h is constant on the considered interval, the equation reads:

$$\begin{aligned} \frac{1}{2}\left(\left\| \dot{\Lambda}_h^{mod,n+1/2} \right\|_2^2 - \left\| \dot{\Lambda}_h^{mod,n-1/2} \right\|_2^2 \right) + \frac{1}{2}\left(\left\| \dot{\Lambda}_h^{mod,n+1/2} \right\|_{\mathbb{D}_h}^2 - \left\| \dot{\Lambda}_h^{mod,n-1/2} \right\|_2^2 \right) = \\ {}^t\mathbb{P}_h F_h^n \cdot \left(\Lambda_h^{mod,n+1/2} - \Lambda_h^{mod,n-1/2} \right) - \int_{t^{n-1/2}}^{t^{n+1/2}} \left\| \dot{\Lambda}_h^{mod} \right\|_{\mathbb{A}_h}^2 \end{aligned} \quad (4.11)$$

The result of the theorem is obtained by simply dividing by Δt. □

4.2 Numerical scheme for the coupled model

We can now deal with the coupling between the string and the soundboard. In order to remain generic, the numerical scheme used for the string is denoted $\mathfrak{C}$. It is assumed to be centred at time t^n, for example 2-IEQ, 2-SAV [Castera and Chabassier, 2023] or the discrete gradient schemes developed in [Chabassier, 2012]. The use of the P-SAV scheme proposed in [Castera and Chabassier, 2023] requires slight adaptation of the schemes to ensure good consistency in $t^{n+1/2}$ by discretizing all variables, including those of the soundboard, onto a single $\{t^n\}$ grid. The 2-SAV scheme that will be used for the following simulations is presented in the appendix A.

Let's start by defining discrete analogues of the positioning vectors ν_c, τ_c and η_c, which we call $\nu_{c,h}$, $\tau_{c,h}$ and $\eta_{c,h}$ such that

$$\forall q_h^* \in \mathcal{Q}_h, \quad \begin{cases} q_h^*(L,t)\cdot\nu_c = Q_h^*\cdot\nu_{c,h} \\ q_h^*(L,t)\cdot\tau_c = Q_h^*\cdot\tau_{c,h} \\ q_h^*(L,t)\cdot\eta_c = Q_h^*\cdot\eta_{c,h} \end{cases} \tag{4.12}$$

and where Q_h^* is the vector of components of q_h^* in the finite element basis of the string.

J_h is the vector that distributes the coupling on the soundboard in a discrete manner

$$\forall i \in [\![1, n_h^\Lambda]\!], \quad (J_h)_i = \oint_{\Omega_h} \chi_\Omega(x,y)\phi_i(x,y)dxdy \tag{4.13}$$

so that

$$\Lambda_h^{EF}\cdot\begin{pmatrix} J_h \\ 0 \\ 0 \end{pmatrix} = \oint_{\Omega_h} u_{p,h}\chi_\Omega \qquad \Lambda_h^{EF}\cdot\begin{pmatrix} 0 \\ J_h \\ 0 \end{pmatrix} = \oint_{\Omega_h} \theta^1_{p,h}\chi_\Omega \qquad \Lambda_h^{EF}\cdot\begin{pmatrix} 0 \\ 0 \\ J_h \end{pmatrix} = \oint_{\Omega_h} \theta^2_{p,h}\chi_\Omega \tag{4.14}$$

With these definitions, the velocity continuity conditions (3.4) can be written at the discrete level

$$\begin{cases} \dot{Q}_h\cdot\nu_{c,h} = \dot{\Lambda}_h^{EF}\cdot\begin{pmatrix} J_h \\ 0 \\ 0 \end{pmatrix} = \dot{\Lambda}_h^{mod}\cdot\ {}^t\mathbb{P}_h\begin{pmatrix} J_h \\ 0 \\ 0 \end{pmatrix} = \dot{\Lambda}_h^{mod}\cdot\ {}^t\mathbb{P}_h^U J_h & \text{(4.15a)} \\ \dot{Q}_h\cdot\tau_{c,h} = \ell\dot{\Lambda}_h^{EF}\cdot\begin{pmatrix} 0 \\ J_h \\ 0 \end{pmatrix} = \ell\dot{\Lambda}_h^{mod}\cdot\ {}^t\mathbb{P}_h\begin{pmatrix} 0 \\ J_h \\ 0 \end{pmatrix} = \dot{\Lambda}_h^{mod}\cdot\ell\ {}^t\mathbb{P}_h^{\Theta 1} J_h & \text{(4.15b)} \\ \dot{Q}_h\cdot\eta_{c,h} = \ell\dot{\Lambda}_h^{EF}\cdot\begin{pmatrix} 0 \\ 0 \\ J_h \end{pmatrix} = \ell\dot{\Lambda}_h^{mod}\cdot\ {}^t\mathbb{P}_h\begin{pmatrix} 0 \\ 0 \\ J_h \end{pmatrix} = \dot{\Lambda}_h^{mod}\cdot\ell\ {}^t\mathbb{P}_h^{\Theta 2} J_h & \text{(4.15c)} \end{cases}$$

where $\mathbb{P}_h^U$, $\mathbb{P}_h^{\Theta 1}$ and $\mathbb{P}_h^{\Theta 2}$ are the transition submatrices associated with the different components $U_{p,h}$, $\Theta^1_{p,h}$ and $\Theta^2_{p,h}$ of the solution vector Λ_h

$$\mathbb{P}_h = \left(\begin{array}{c} \mathbb{P}_h^U \\ \hline \mathbb{P}_h^{\Theta 1} \\ \hline \mathbb{P}_h^{\Theta 2} \end{array}\right) \qquad {}^t\mathbb{P}_h = \left(\begin{array}{c|c|c} {}^t\mathbb{P}_h^U & {}^t\mathbb{P}_h^{\Theta 1} & {}^t\mathbb{P}_h^{\Theta 2} \end{array}\right)$$

Numerical scheme 4.2 (Coupling string - soundboard)

At each and every iteration, seek $Q_h^{n+1} \in \mathbb{R}^{n_h^q}$, $\Lambda_h^{mod,n+1/2} \in \mathbb{R}^{n_h^\Lambda}$ and $(F^P, G^P, H^P) \in \mathbb{R}^3$ so that

String scheme:

$$\mathfrak{C}(Q_h^{n+1}, Q_h^n, Q_h^{n-1}) = F_h^n + F^P \nu_{c,h} + G^P \tau_{c,h} + H^P \eta_{c,h} \tag{4.16a}$$

Coupling scheme:

$$\begin{cases} \dfrac{Q_h^{n+1} - Q_h^{n-1}}{2\Delta t} \cdot \nu_{c,h} = \dfrac{\Lambda_h^{mod,n+1/2} - \Lambda_h^{mod,n-1/2}}{\Delta t} \cdot {}^t\mathbb{P}_h^U J_h \\ \dfrac{Q_h^{n+1} - Q_h^{n-1}}{2\Delta t} \cdot \tau_{c,h} = \dfrac{\Lambda_h^{mod,n+1/2} - \Lambda_h^{mod,n-1/2}}{\Delta t} \cdot \ell\, {}^t\mathbb{P}_h^{\Theta 1} J_h \\ \dfrac{Q_h^{n+1} - Q_h^{n-1}}{2\Delta t} \cdot \eta_{c,h} = \dfrac{\Lambda_h^{mod,n+1/2} - \Lambda_h^{mod,n-1/2}}{\Delta t} \cdot \ell\, {}^t\mathbb{P}_h^{\Theta 2} J_h \end{cases} \tag{4.16b}$$

Soundboard scheme:

$$\begin{cases} \forall t \in [t^{n-1/2}, t^{n+1/2}], \quad \ddot{\Lambda}_h^{mod}(t) + \mathbb{A}_h \dot{\Lambda}_h^{mod}(t) + \mathbb{D}_h \Lambda_h^{mod}(t) = {}^t\mathbb{P}_h F_h^n \\ \qquad\qquad = -F^P\, {}^t\mathbb{P}_h^U J_h - G^P \ell\, {}^t\mathbb{P}_h^{\Theta 1} J_h - H^P \ell\, {}^t\mathbb{P}_h^{\Theta 2} J_h \\ \Lambda_h^{mod}(t^{n-1/2}) = \Lambda_h^{mod,n-1/2}, \quad \dot{\Lambda}_h^{mod}(t^{n-1/2}) = \dot{\Lambda}_h^{mod,n-1/2} \end{cases} \tag{4.16c}$$

Theorem 4.2 (Discrete power balance of the scheme 4.2)

The solution to the scheme 4.2 verifies

$$\begin{cases} \dfrac{\mathcal{E}_{c,p}^{n+1/2} - \mathcal{E}_{c,p}^{n-1/2}}{\Delta t} = F_h^n \cdot \dfrac{Q_h^{n+1} - Q_h^{n-1}}{2\Delta t} \\ \qquad\qquad - \left\| \dfrac{Q_h^{n+1} - Q_h^{n-1}}{2\Delta t} \right\|_{R_h}^2 - \dfrac{1}{\Delta t} \displaystyle\int_{t^{n-1/2}}^{t^{n+1/2}} \left\| \dot{\Lambda}_h^{mod} \right\|_{\mathbb{A}_h}^2 \end{cases} \tag{4.17a}$$

$$\mathcal{E}_{c,p}^{n+1/2} = \mathcal{E}_c^{n+1/2} + \mathcal{E}_p^{n+1/2} \tag{4.17b}$$

where $\mathcal{E}_c$ is the discrete scheme-dependent energy of the string. See for example the theorem A.3 for the 2-SAV scheme. $\mathcal{E}_p$ is the soundboard energy defined by the theorem 4.1.

Proof. The proof is similar to that of the continuous theorem 4.2: all coupling terms simplify to guarantee exact coupling in terms of energy exchange. □

4.3 Solving algorithm

The 4.2 scheme discretizes the coupling equations implicitly.
That being said, it is possible to make the resolution method explicit by using the equation (4.8a):

$$\begin{cases} \dfrac{Q_h^{n+1}-Q_h^{n-1}}{2}\cdot\nu_{c,h} = \left(\mathcal{S}^0_{\Delta t}\Lambda_h^{mod,n-1/2} + \mathcal{S}^1_{\Delta t}\dot{\Lambda}_h^{mod,n-1/2} + \mathcal{R}_{\Delta t}\,{}^t\mathbb{P}_h F_h^n - \Lambda_h^{mod,n-1/2}\right)\cdot\,{}^t\mathbb{P}_h^U J_h \\ \dfrac{Q_h^{n+1}-Q_h^{n-1}}{2}\cdot\tau_{c,h} = \left(\mathcal{S}^0_{\Delta t}\Lambda_h^{mod,n-1/2} + \mathcal{S}^1_{\Delta t}\dot{\Lambda}_h^{mod,n-1/2} + \mathcal{R}_{\Delta t}\,{}^t\mathbb{P}_h F_h^n - \Lambda_h^{mod,n-1/2}\right)\cdot\ell\,{}^t\mathbb{P}_h^{\Theta 1} J_h \\ \dfrac{Q_h^{n+1}-Q_h^{n-1}}{2}\cdot\eta_{c,h} = \left(\mathcal{S}^0_{\Delta t}\Lambda_h^{mod,n-1/2} + \mathcal{S}^1_{\Delta t}\dot{\Lambda}_h^{mod,n-1/2} + \mathcal{R}_{\Delta t}\,{}^t\mathbb{P}_h F_h^n - \Lambda_h^{mod,n-1/2}\right)\cdot\ell\,{}^t\mathbb{P}_h^{\Theta 2} J_h \end{cases}$$

Let us introduce

$$F_\Lambda^{n-1/2} = \mathcal{S}^0_{\Delta t}\Lambda_h^{mod,n-1/2} + \mathcal{S}^1_{\Delta t}\dot{\Lambda}_h^{mod,n-1/2} \tag{4.18}$$

which allows the coupling conditions to be rewritten in explicit form:

$$\begin{cases} \dfrac{Q_h^{n+1}-Q_h^{n-1}}{2}\cdot\nu_{c,h} = \mathcal{A}_1^{n-1/2} - F^P\mathcal{B}_{1,1} - G^P\mathcal{B}_{1,2} - H^P\mathcal{B}_{1,3} & \text{(4.19a)} \\ \dfrac{Q_h^{n+1}-Q_h^{n-1}}{2}\cdot\tau_{c,h} = \mathcal{A}_2^{n-1/2} - F^P\mathcal{B}_{2,1} - G^P\mathcal{B}_{2,2} - H^P\mathcal{B}_{2,3} & \text{(4.19b)} \\ \dfrac{Q_h^{n+1}-Q_h^{n-1}}{2}\cdot\eta_{c,h} = \mathcal{A}_3^{n-1/2} - F^P\mathcal{B}_{3,1} - G^P\mathcal{B}_{3,2} - H^P\mathcal{B}_{3,3} & \text{(4.19c)} \end{cases}$$

where $\mathcal{A}^{n-1/2}$ is the vector defined by

$$\mathcal{A}^{n-1/2} = \begin{pmatrix} \left(F_\Lambda^{n-1/2} - \Lambda_h^{mod,n-1/2}\right)\cdot\,{}^t\mathbb{P}_h^U J_h \\ \left(F_\Lambda^{n-1/2} - \Lambda_h^{mod,n-1/2}\right)\cdot\ell\,{}^t\mathbb{P}_h^{\Theta 1} J_h \\ \left(F_\Lambda^{n-1/2} - \Lambda_h^{mod,n-1/2}\right)\cdot\ell\,{}^t\mathbb{P}_h^{\Theta 2} J_h \end{pmatrix} \tag{4.20}$$

and $\mathcal{B}$ the constant matrix

$$\mathcal{B} = \mathcal{R}_{\Delta t}\begin{pmatrix} {}^t\mathbb{P}_h^U J_h\cdot\,{}^t\mathbb{P}_h^U J_h & \ell\,{}^t\mathbb{P}_h^{\Theta 1} J_h\cdot\,{}^t\mathbb{P}_h^U J_h & \ell\,{}^t\mathbb{P}_h^{\Theta 2} J_h\cdot\,{}^t\mathbb{P}_h^U J_h \\ {}^t\mathbb{P}_h^U J_h\cdot\ell\,{}^t\mathbb{P}_h^{\Theta 1} J_h & \ell\,{}^t\mathbb{P}_h^{\Theta 1} J_h\cdot\ell\,{}^t\mathbb{P}_h^{\Theta 1} J_h & \ell\,{}^t\mathbb{P}_h^{\Theta 2} J_h\cdot\ell\,{}^t\mathbb{P}_h^{\Theta 1} J_h \\ {}^t\mathbb{P}_h^U J_h\cdot\ell\,{}^t\mathbb{P}_h^{\Theta 2} J_h & \ell\,{}^t\mathbb{P}_h^{\Theta 1} J_h\cdot\ell\,{}^t\mathbb{P}_h^{\Theta 2} J_h & \ell\,{}^t\mathbb{P}_h^{\Theta 2} J_h\cdot\ell\,{}^t\mathbb{P}_h^{\Theta 2} J_h \end{pmatrix} \tag{4.21}$$

The method for solving the 4.2 scheme, which treats the string and soundboard decoupled, is then summarized by the following algorithm:

$$
\begin{cases}
\text{Initialize all the variables and pre-compute } \mathcal{S}^0_{\Delta t},\ \mathcal{S}^1_{\Delta t},\ \mathcal{R}_{\Delta t} \text{ and } \mathcal{B} \\
\text{For each and every iteration:} \\
\quad \text{- Update } F_\Lambda^{n-1/2} \text{ and } \mathcal{A}^{n-1/2} \\
\quad \text{- Solve the string's scheme with the coupling conditions:} \\
\qquad \begin{cases}
\mathfrak{C}(Q_h^{n+1}, Q_h^n, Q_h^{n-1}) = S_h^n + F^P \nu_{c,h} + G^P \tau_{c,h} + H^P \eta_{c,h} \\
\dfrac{Q_h^{n+1} - Q_h^{n-1}}{2} \cdot \nu_{c,h} = \mathcal{A}_1^{n-1/2} - F^P \mathcal{B}_{1,1} - G^P \mathcal{B}_{1,2} - H^P \mathcal{B}_{1,3} \\
\dfrac{Q_h^{n+1} - Q_h^{n-1}}{2} \cdot \tau_{c,h} = \mathcal{A}_2^{n-1/2} - F^P \mathcal{B}_{2,1} - G^P \mathcal{B}_{2,2} - H^P \mathcal{B}_{2,3} \\
\dfrac{Q_h^{n+1} - Q_h^{n-1}}{2} \cdot \eta_{c,h} = \mathcal{A}_3^{n-1/2} - F^P \mathcal{B}_{3,1} - G^P \mathcal{B}_{3,2} - H^P \mathcal{B}_{3,3}
\end{cases} \qquad (4.22a) \\
\quad \text{- Update the soundboard unknowns:} \\
\qquad \Lambda_h^{mod,n+1/2} = F_\Lambda^{n-1/2} - F^P \mathcal{R}_{\Delta t}\, {}^t\mathbb{P}_h^U J_h - G^P \mathcal{R}_{\Delta t} \ell\, {}^t\mathbb{P}_h^{\Theta 1} J_h - H^P \mathcal{R}_{\Delta t} \ell\, {}^t\mathbb{P}_h^{\Theta 2} J_h \qquad (4.22b)
\end{cases}
$$

4.4 Numerical results

In this section, we present comparisons between the refined model with three degrees of freedom in the $\vec{\nu}$, $\vec{\tau}$ and $\vec{\eta}$ directions, hereafter referred to as "3dof", and the [Chabassier, 2012] model where the bridge has only one degree of freedom in the $\vec{\nu}$ direction, hereafter referred to as "1dof".
Note that the β angle has no influence on the 1dof model, for which it is always set to 0, and the H^P multiplier is eliminated.
After a paragraph on calculating the soundboard modes, we check the energy conservation and convergence properties of the new scheme.

The parameters used for the following simulations are summarized below. In place of the hammer, the geometrically exact and stiffness-free string F_3 is excited by a $\mathscr{C}^\infty$ source in space and time as defined by appendix B.

String's scheme						
Scheme	N_x	θ	Order	Auxiliary constant	Stabilization	Damping
2-SAV	11	1/4	4	10^4	α^*	No

Source term				
A [-]	x_0 [m]	σ_x [m]	t_0 [ms]	σ_t [ms]
10000	0,115	0,01	2,5	1,5

Table 1: Discretization parameters for the string.

The soundboard is a 9-millimeter-thick spruce plate whose wood fibers are oriented at an angle of $\beta = 54.4°$. 16 spruce stiffeners, also oriented at $\beta = -40°$ and 25 millimeters thick, are glued to it. They are shown in green of the adjacent drawing. The pink bridge of 40 mm high, is made of beech. These thickness variations are taken into account by locally changing the thickness of the Reissner-Mindlin plate.

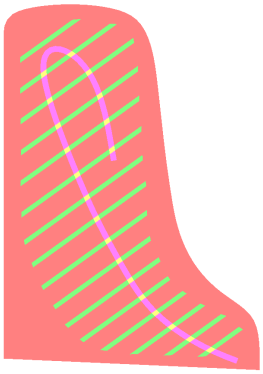

Wood	ρ [kg.m^{-3}]	E_{xx} [GPa]	E_{yy} [GPa]	ν_{xy} [-]	ν_{yx} [-]	G_{xy} [GPa]	G_{xz} [GPa]	G_{yz} [GPa]
Spruce	380	11,0	0,65	0,26	0,015	0,66	1,2	0,042
Beech	750	13,7	2,24	0,3	0	1,61	1,06	0,46

Table 2: Mechanical parameters for the soundboard.

The parameters used to model the soundboard damping in simulations where it is taken into account are such that (see paragraph 2.2)

$$f_{ve}(f) = 2 \times 10^{-5} f^2 + 7 \times 10^{-2} f \tag{4.23}$$

4.4.a Computation of the modes

the modes of the soundboard are computed by the Arpack[1] software from a 2D mesh and with 4-th order finite elements.

Although the mesh in figure 4 is composed of triangles and quadrangles, the Montjoie[2] finite element code automatically cuts triangles into quadrangles to obtain a purely quadrangular mesh and allow mass lumping. This increases the solver's efficiency, as the mass matrix $\mathbb{M}_h$ doesn't have to be factorized. In figure 4, the stiffeners are shown in green, and the bridge in pink.

Some modal deformations from simulations are shown in figure 5. They are consistent with the Chladni shapes obtained experimentally in [Conklin, 1996] as well as those measured and simulated in step 3 of [Corradi et al., 2017].
The influence of the stiffeners and bridge can be seen in figure 5 in the form of hatched patterns clearly visible on certain angular modes (modes 2, 3 and 7).

Finally, it should be noted that the computation of some 2,500 modes is required to reach the 10 kHz frequency.

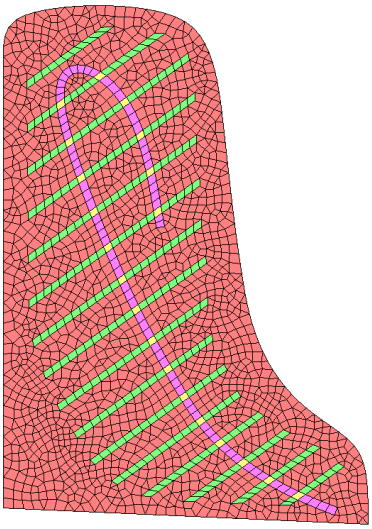

Figure 4: 2D-mesh of the soundboard.

[1] `https://en.wikipedia.org/wiki/ARPACK`
[2] `https://www.math.u-bordeaux.fr/~durufle/montjoie/`

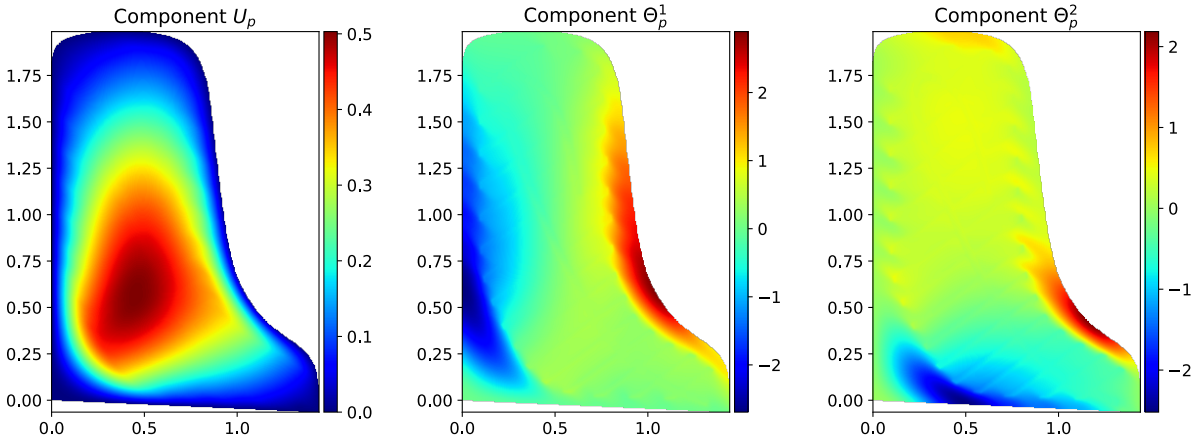

(a) Mode 1 (27 Hz)

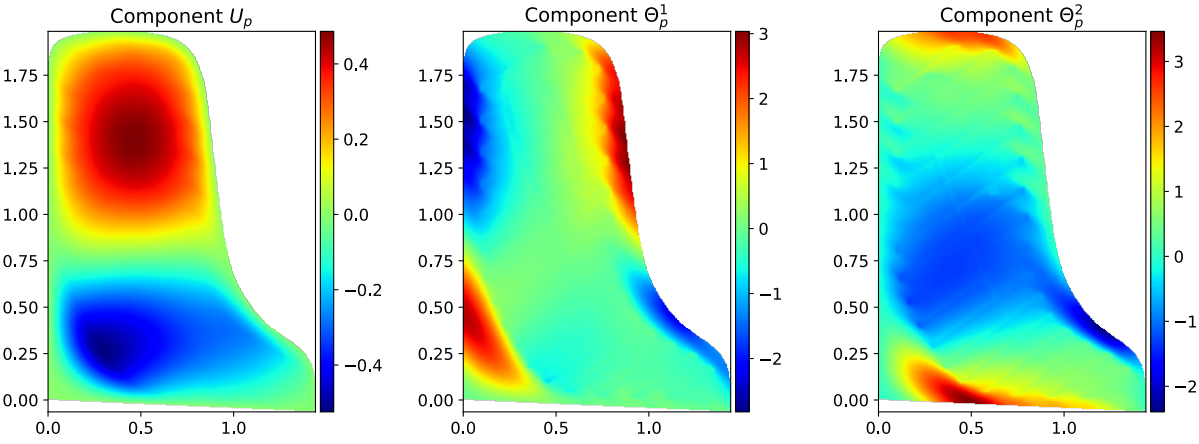

(b) Mode 2 (42 Hz)

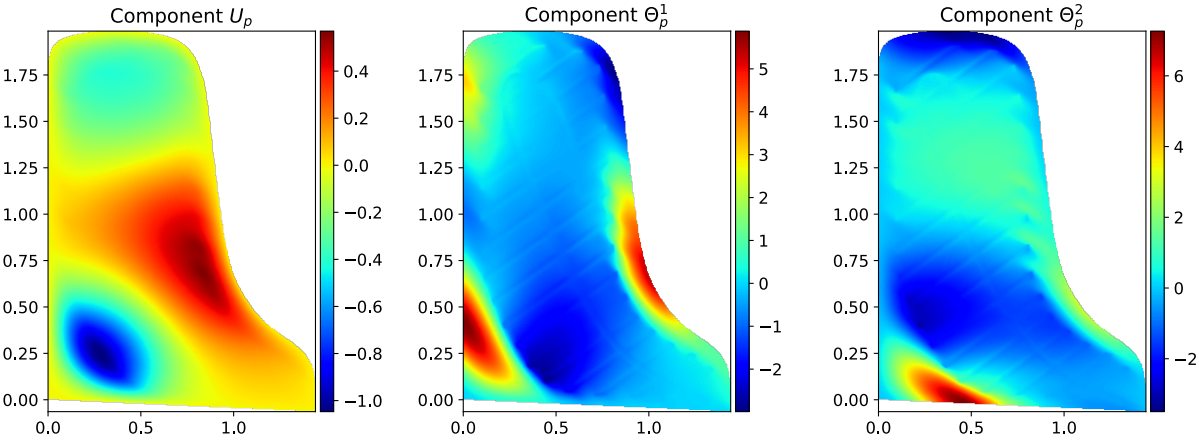

(c) Mode 3 (63 Hz)

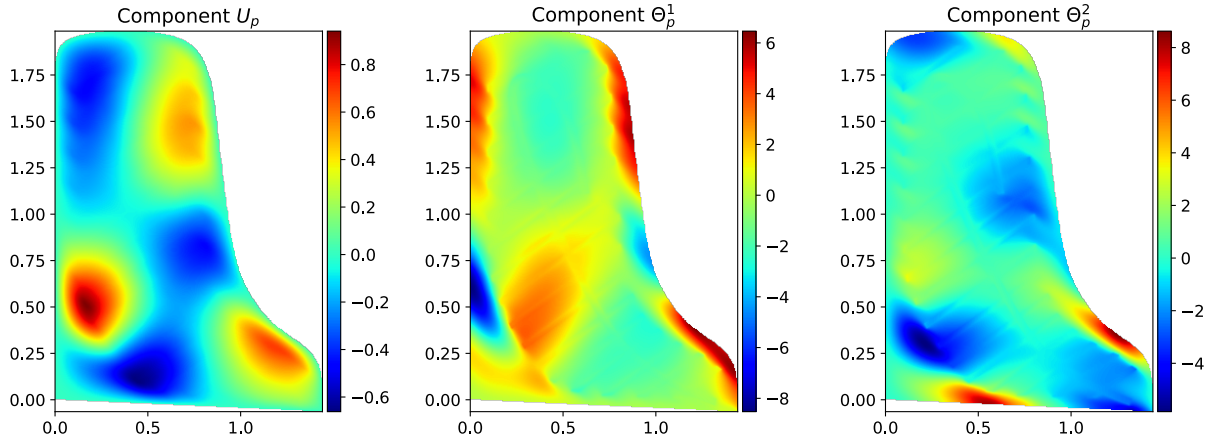

(d) Mode 7 (121 Hz)

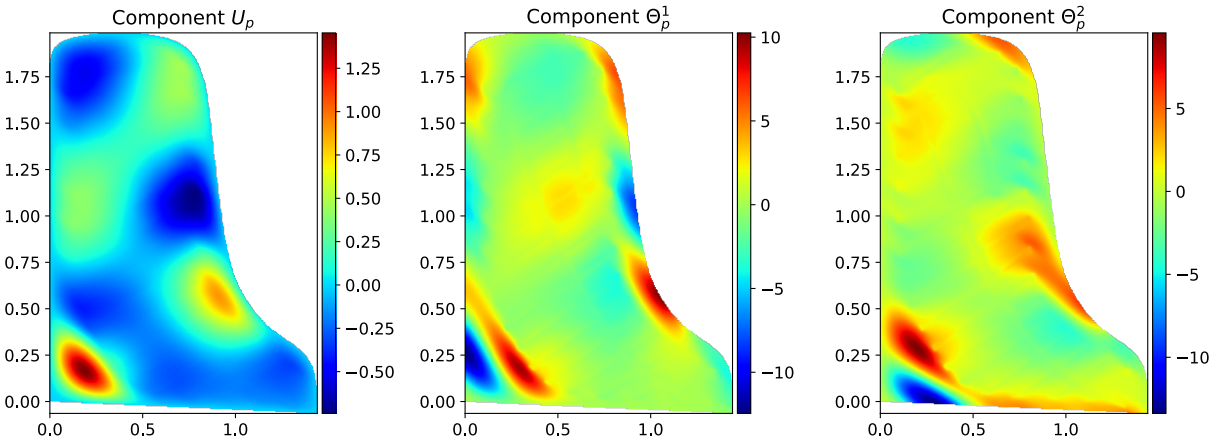

(e) Mode 10 (164 Hz)

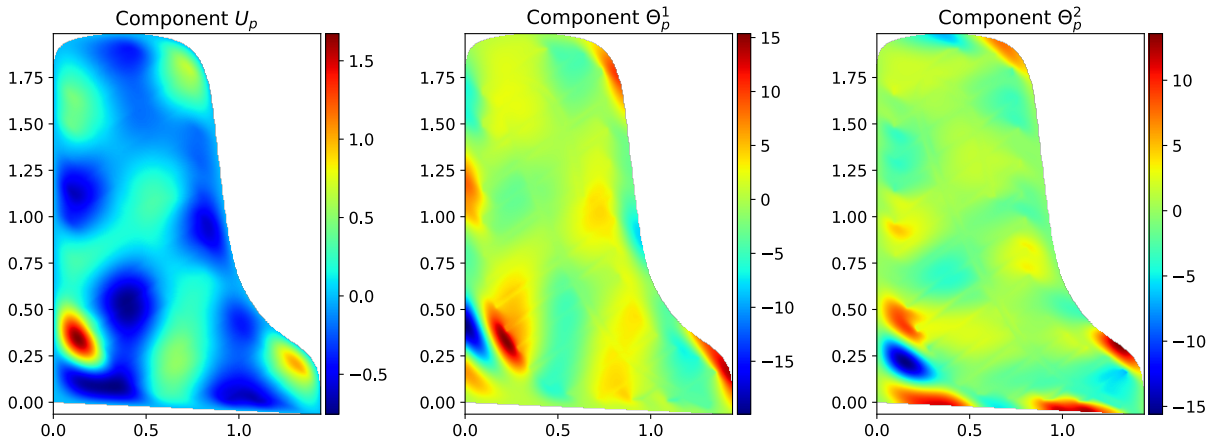

(f) Mode 20 (289 Hz)

Figure 5: Modal soundboard deformations. Membrane component (left) and shear angles (center, right).

4.4.b Numerical preservation of the power balance

In the absence of damping and for $\alpha = 45°$ and $\beta = 45°$, we define the energy residual ε in relation to the theorem 4.2 as

$$\varepsilon = \frac{\mathcal{E}_{c,p}^{n+1/2} - \mathcal{E}_{c,p}^{n-1/2}}{\mathcal{E}_{max}} - F_h^n \cdot \frac{Q_h^{n+1} - Q_h^{n-1}}{2\mathcal{E}_{max}} \tag{4.24}$$

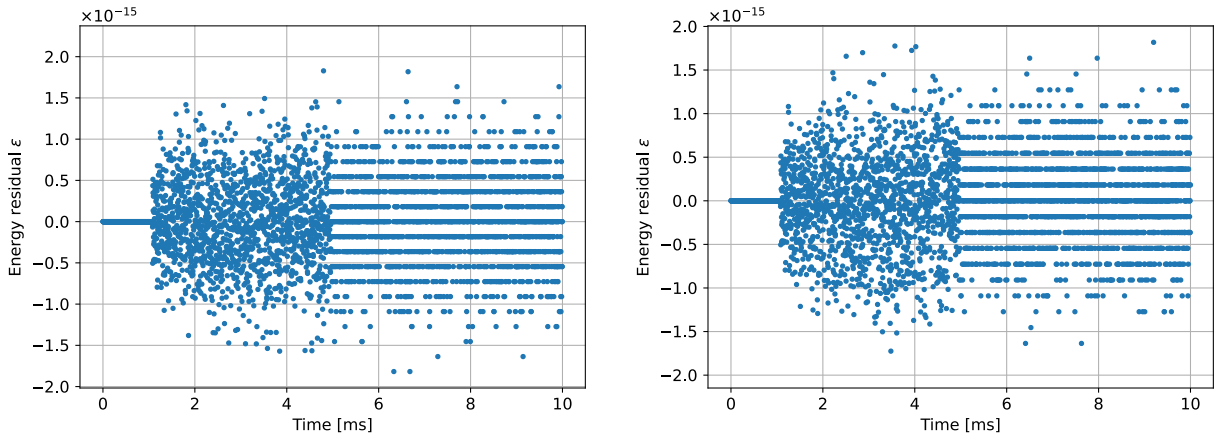

Figure 6: Energy residual for 1dof (left) and 3dof (right) transmission.

It is clear from figure 6 that the ε energy residuals are multiples of the machine error. The discrete power balance is therefore verified.

4.4.c Time convergence of the scheme

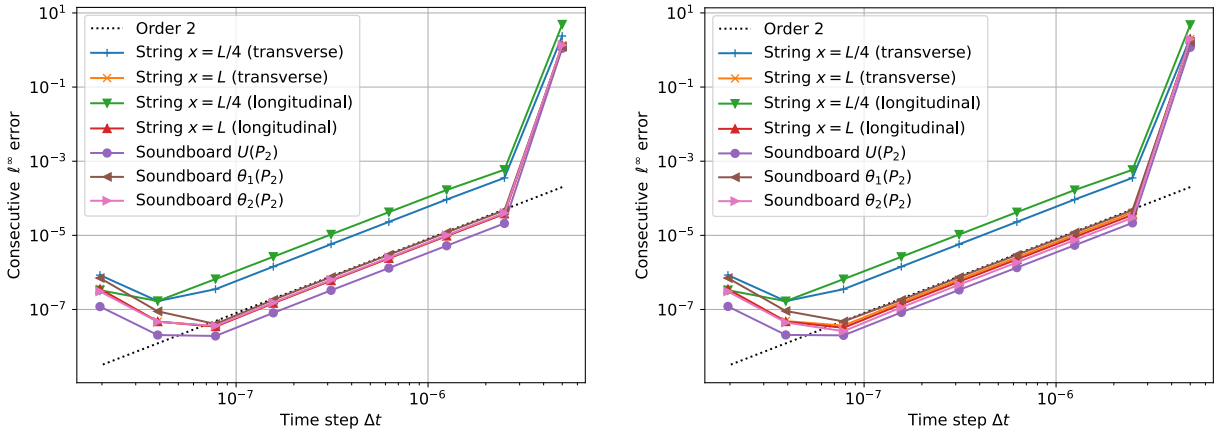

Figure 7: Time convergence for 1dof (left) and 3dof (right) transmission.

Figure 7 shows time convergence curves of the 4.2 scheme for the 1dof transmission model and the 3dof refinement. Errors are calculated in ℓ^∞ norm by dividing the time step consecutively by 2 and at specific positions on the string ($x = L/4$ and $x = L$) and on the table (P_2 position).

$$\forall (X, Y) \in \mathbb{R}^n \times \mathbb{R}^n, \quad E_{\ell^\infty}(X, Y) = \frac{\|X - Y\|_\infty}{\|Y\|_\infty} = \frac{\max\limits_{i \in [\![1,n]\!]} |x^i - y^i|}{\max\limits_{i \in [\![1,n]\!]} |y^i|} \tag{4.25}$$

Apart from the first point with a large time step, which is heavily polluted due to the 2-SAV string scheme as described in [Castera and Chabassier, 2023], the convergence is quadratic. An increase in error, also described in [Castera and Chabassier, 2023] and typical of the 2-SAV method, is visible for small time steps.

5 Transmission of longitudinal waves and precursors

Let us remember that transverse and longitudinal waves have very different propagation velocities in the strings. Longitudinal waves usually travel about 15 times faster than transverse waves, giving rise to the longitudinal precursor phenomenon observed in [Podlesak and Lee, 1988].
The greater the difference between the arrival times of the two waves at the bridge, the more visible the precursor.
In this section, we keep on considering a non-linear string with no stiffness, excited by a regular source that produces a *fortissimo* nuance. Stiffness is not taken into account in order to observe only longitudinal phenomena without polluting them with dispersive phenomena. We show results on a low $D_1^\sharp$ string, a medium F_3 string about half as long, and an even shorter high $C_5^\sharp$ string. We add damping in the strings and in the soundboard, and the string mesh uses $N_x = 70$ nodes.

5.1 $D_1^\sharp$ note

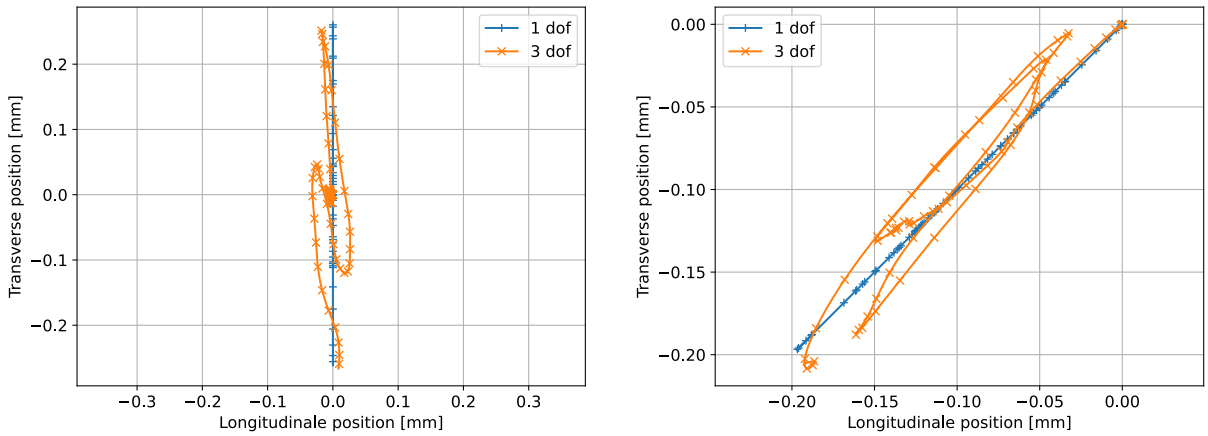

Figure 8: Motion of the end of the string with $\alpha = 0$ (left) and $\alpha = 45°$ (right).

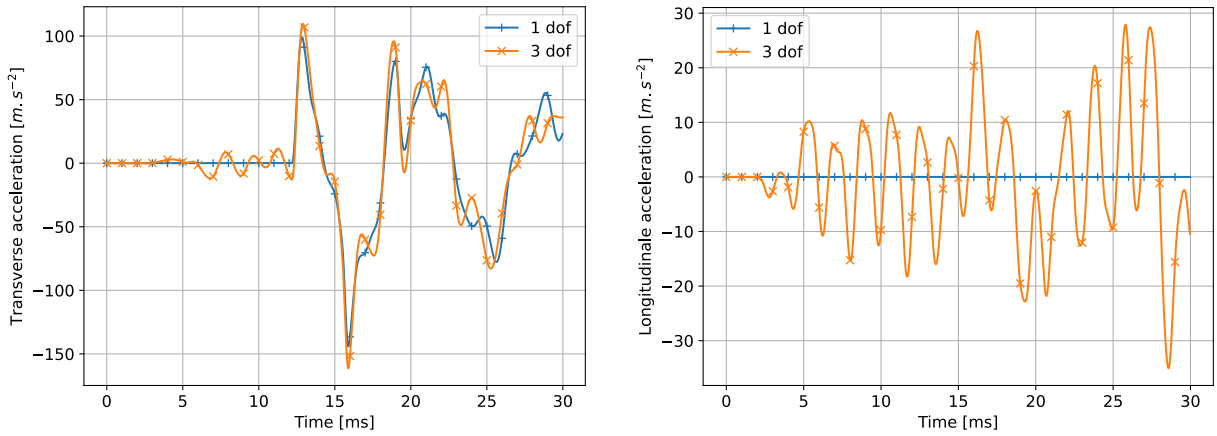

Figure 9: Acceleration of the end of the string for $\alpha = 0$. Transverse (left), longitudinal (right).

Figure 8 shows the different positions taken by the $x = L$ end of the string. On the left, for a 1dof transmission, the string is constrained vertically along the $\vec{\nu}$ axis. With 3dof, the movement is no longer strictly vertical, and a longitudinal component appears. In the figure on the right, with an angle $\alpha = 45°$, we can make the same observations, but in a frame rotated by 45°, consistent with the string's orientation.

Figure 9 shows the acceleration of the $x = L$ end of the string attached to the bridge in its transverse direction on the left and its longitudinal direction on the right for an angle $\alpha = 0$. With a 1dof transmission, everything happens as if the string were subject to a Dirichlet condition in the longitudinal direction. As it can be seen in the figure on the right, the $x = L$ end of the string has no mobility in the longitudinal direction, and only the transverse component visible in the figure on the left starting at 12 ms can be transmitted.
With 3dof transmission, the string is free to move in its longitudinal direction, as it can be seen on the right-hand figure 9. Since longitudinal waves propagate much faster than transverse waves, the first longitudinal vibrations appear at 2 ms, i.e. much faster than the first transverse vibrations that were visible with 1dof. Consequently, the vibrations in the interval [2 ms, 12 ms] are entirely due to longitudinal phenomena, whether caused by the longitudinal waves themselves in the figure on the right, or by their non-linear coupling with the transverse waves in the figure on the left. The vibratory signal between 2 ms and 12 ms is a longitudinal precursor.

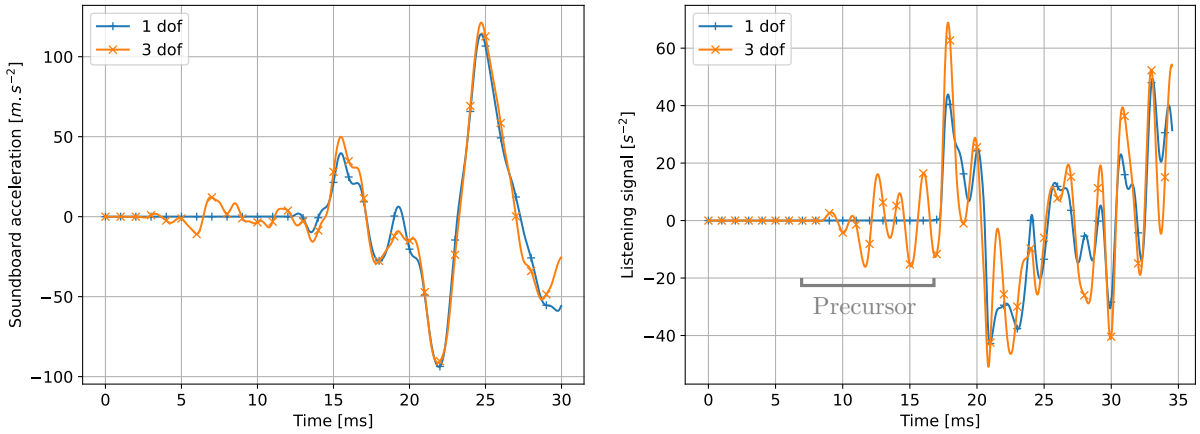

Figure 10: Soundboard acceleration at P_1 (left). Listening signal (right).

The same phenomena are visible on the soundboard and illustrated in figure 10. The figure on the left shows the acceleration of point P_1 on the soundboard, and that on the right a listening signal reconstructed by combining several points on the soundboard and recorded at a point distant from the piano (see appendix D). With a 1dof transmission, the first waves are visible from 12 ms at point P_1 and delayed to 17 ms at the listening point due to its distance. With 3dof transmission, waves are visible from 2 ms at point P_1, and from 7 ms at the listening point. The additional vibrations constitute the longitudinal precursor that is potentially audible at the sound attack, given its high amplitude.

The power spectrum of the listening signal is shown in figure 11. Fairly significant amplitude differences can be observed along the entire frequency range, but specifically marked on the longitudinal partials, which are influenced by the presence of the precursor.

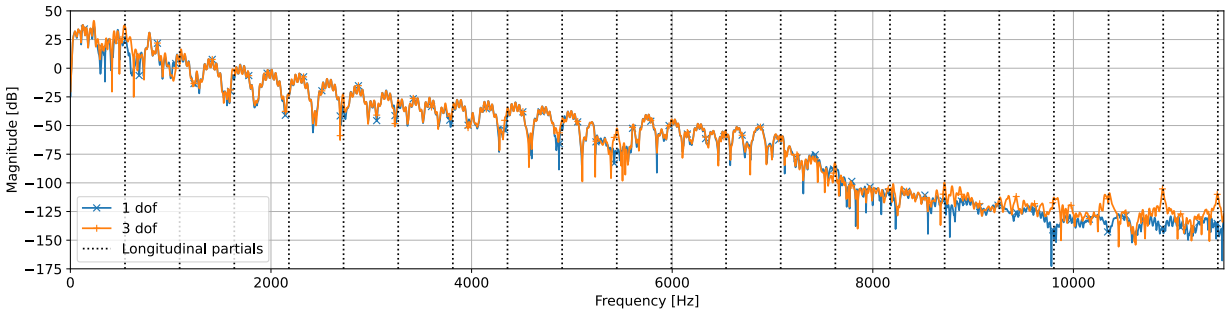

Figure 11: Power spectrum of the listening signal.

5.2 F_3 note

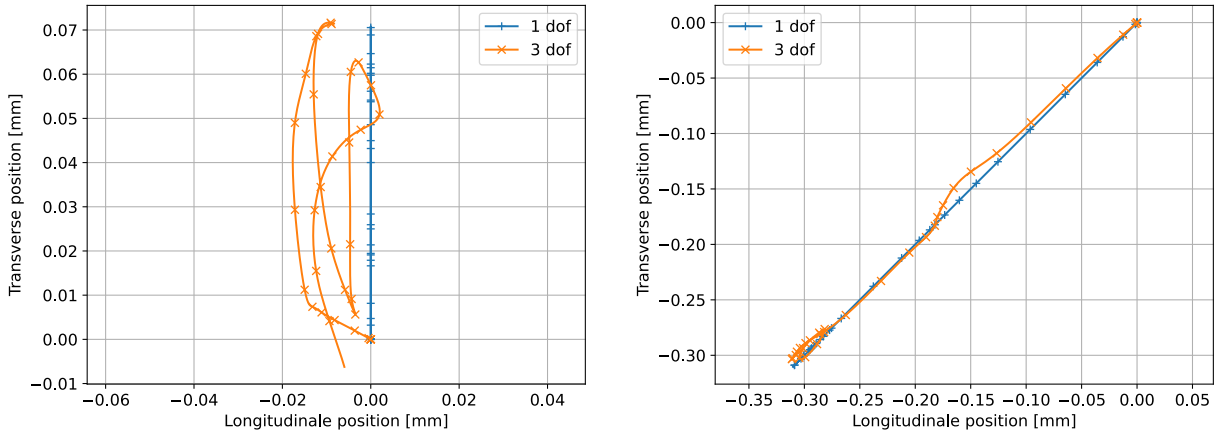

Figure 12: Motion of the end of the string with $\alpha = 0$ (left) and $\alpha = 45°$ (right).

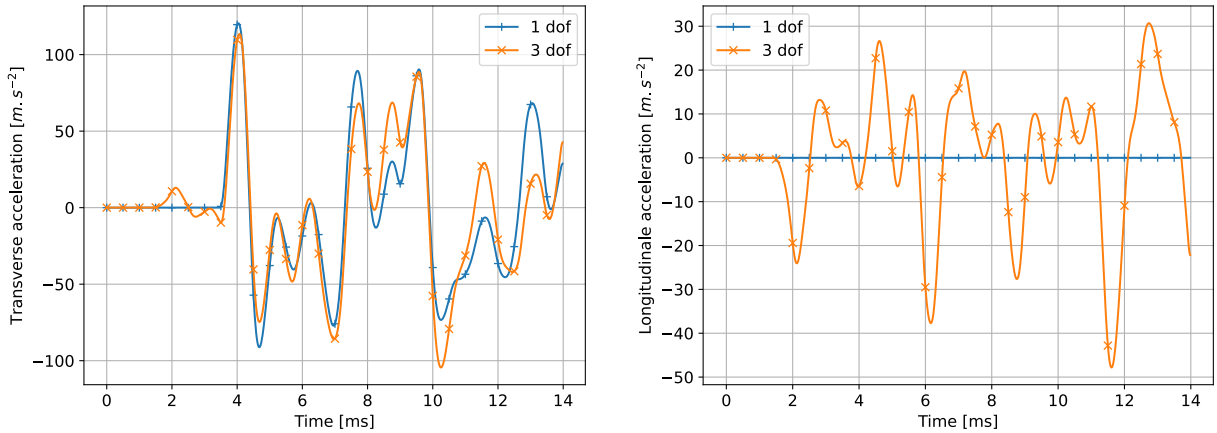

Figure 13: Acceleration of the end of the string for $\alpha = 0$. Transverse (left), longitudinal (right).

The observations made on the note $D_1^\sharp$ remain valid, but the precursor is less visible and shorter (less than 2 ms) due to the reduced string length. The power spectrum of the listening signal in figure 15 shows fairly significant differences, most pronounced on the longitudinal partials.

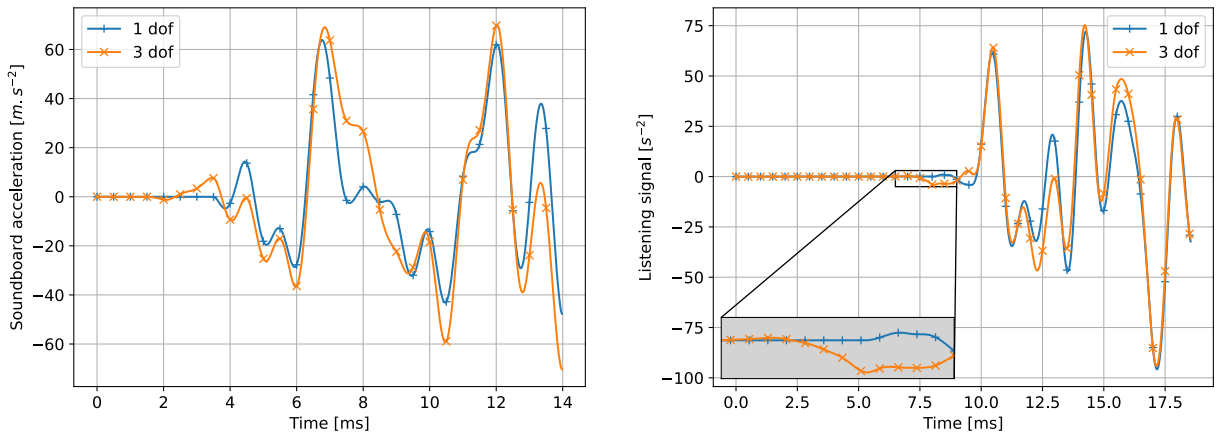

Figure 14: Soundboard acceleration at P_1 (left). Listening signal (right).

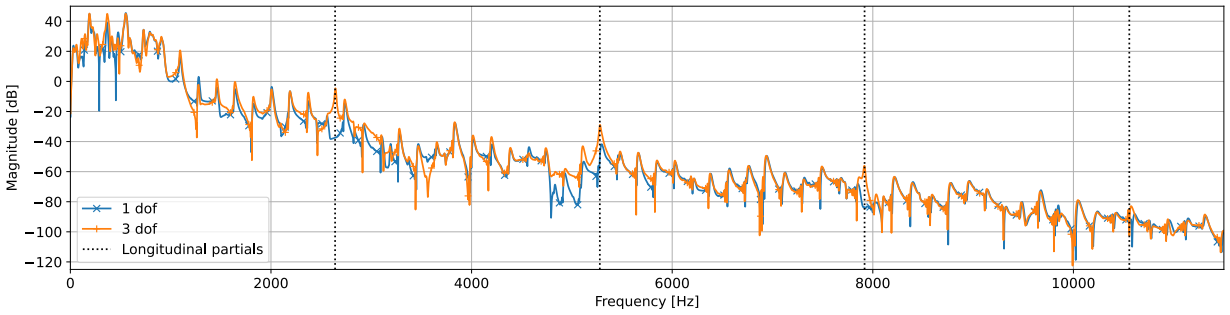

Figure 15: Power spectrum of the listening signal.

5.3 $C_5^{\sharp}$ note

For this note, due to its short length ($L = 32.6$ cm), we use a less refined string mesh with $N_x = 20$ nodes.

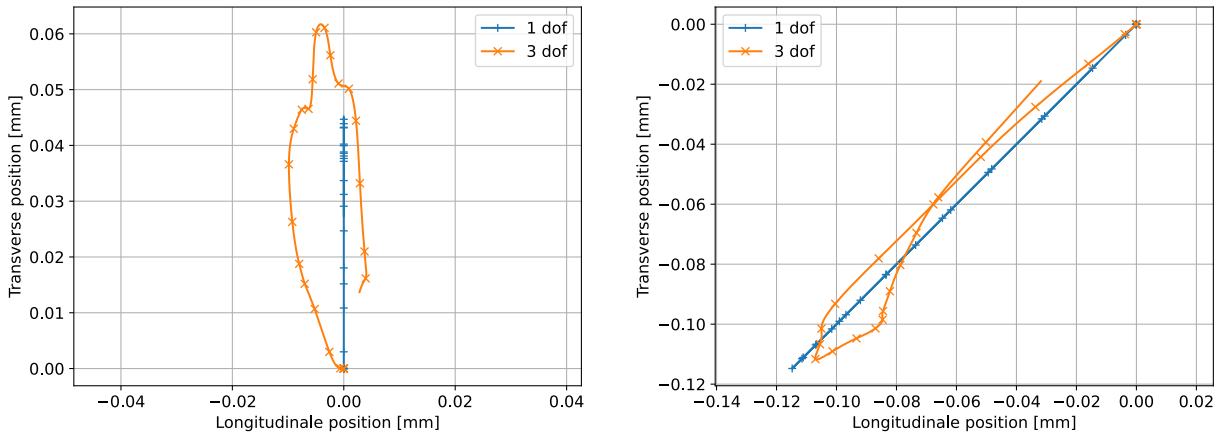

Figure 16: Motion of the end of the string with $\alpha = 0$ (left) and $\alpha = 45°$ (right).

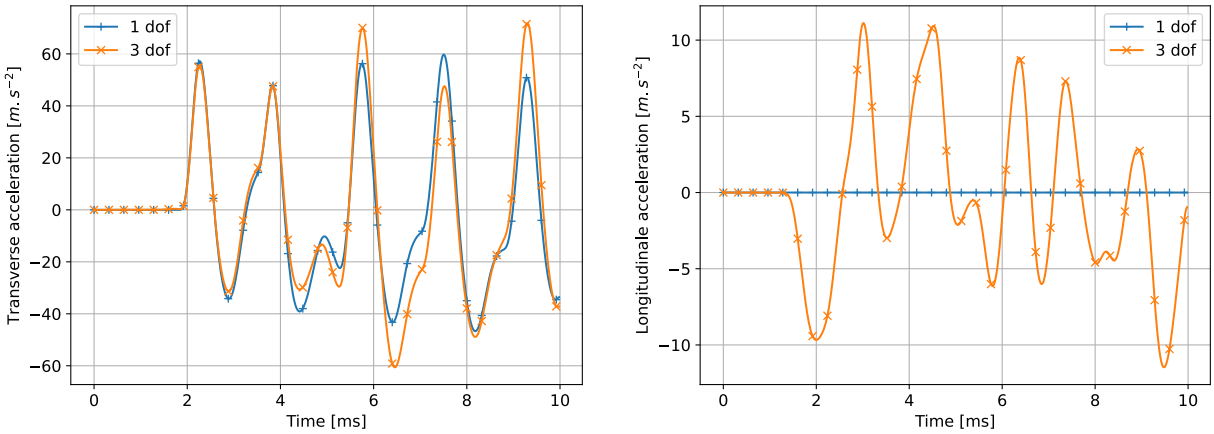

Figure 17: Acceleration of the end of the string for $\alpha = 0$. Transverse (left), longitudinal (right).

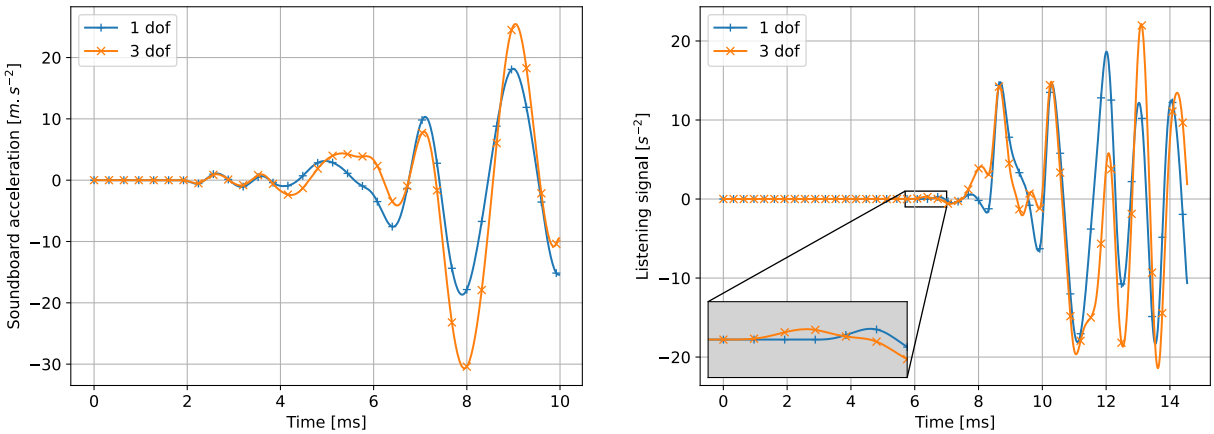

Figure 18: Soundboard acceleration at P_1 (left). Listening signal (right).

Here again, the precursor exists, but has no oscillations of its own and lasts less than a millisecond, which is coherent with the short length of the string. The power spectrum of the listening signal is again quite strongly modified.

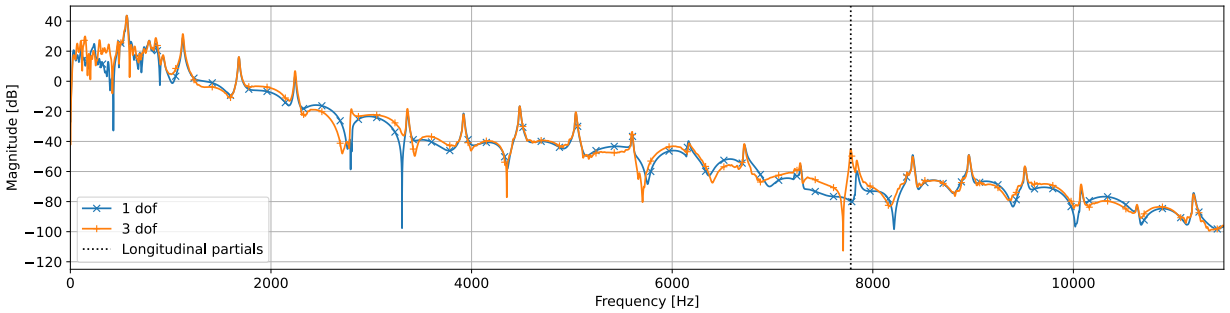

Figure 19: Power spectrum of the listening signal.

5.4 Summary

The model developed allows us to account for complex bridge movements in the soundboard elevation and shear directions, and also shows the presence of longitudinal precursors throughout the piano range. Their amplitude and duration are consistent with string length: the longer the strings, the longer the precursors and the higher their amplitude. Their importance decreases rapidly with string length.

Beyond the presence of precursors, there are also very significant differences between signals with and without transmission. Spectral contents are significantly different, mainly in longitudinal resonances.

6 Influence of the string orientation relatively to the soundboard

Due to the presence of the oriented stiffeners, the bridge and the anisotropic properties of wood, it is possible that the orientation of the strings relatively to the soundboard has an effect on the transmission of waves at the bridge. This is studied in this section.

To do this, we study the admittance of the bridge, i.e. the possible mobility in the three free directions $(\vec{\nu}, \vec{\eta}, \vec{\tau})$ as a function of frequencies and as a function of the lateral angle β defined by figure 2.

6.1 Bridge admittance - Frequency mobility

Let us go back to the equation that describes the soundboard's vibrations

$$\mathbb{M}\ddot{\Lambda}_p + f_{ve}(\mathbb{R})\dot{\Lambda} + \mathbb{R}\Lambda_p = F(x,y,t) \tag{6.1}$$

and apply a Fourier transform to study it in the frequency domain

$$\left(-\omega^2\mathbb{M} + i\omega f_{ve}(\mathbb{R}) + \mathbb{R}\right)\hat{\Lambda}_p = \hat{F}(x,y,\omega) \tag{6.2}$$

The bridge admittance matrix [Chaigne and Kergomard, 2008], [Cuenca and Caussé, 2007] defined by

$$\hat{\mathbb{Y}}(\omega)\hat{F}(x,y,\omega) = i\omega\hat{\Lambda}_p(x,y,\omega) \tag{6.3}$$

writes

$$\hat{\mathbb{Y}}(\omega) = i\omega\left(\mathbb{R} + i\omega f_{ve}(\mathbb{R}) - \omega^2\mathbb{M}\right)^{-1} \tag{6.4}$$

The same reasoning on the discrete modal problem gives an admittance matrix

$$\hat{\mathbb{Y}}_h(\omega) = i\omega\left(\mathbb{D}_h + i\omega\mathbb{A}_h - \omega^2\mathbb{I}_h\right)^{-1} \tag{6.5}$$

For each pulse ω, this matrix characterizes the soundboard's mobility as a function of the input force applied to it. Of course, this input force depends on the relative orientation of the string and the soundboard.

6.2 Power transmitted to the soundboard

The instantaneous power transmitted through the bridge is given by

$$\mathcal{P}(t) = \int_\Omega F(x,y,t)\cdot\dot{\Lambda}_p(x,y,t)dxdy \tag{6.6}$$

and Parseval's formula ensures equivalence of norms between the time domain and the Fourier domain:

$$\int_{\mathbb{R}^+}\mathcal{P}(t)dt = \int_{\mathbb{R}}\mathcal{P}(t)dt = \frac{1}{2\pi}\int_{\mathbb{R}}\int_\Omega \hat{F}^*(x,y,\omega)\cdot i\omega\hat{\Lambda}_p(x,y,\omega)dxdyd\omega = \frac{1}{2\pi}\int_{\mathbb{R}}\hat{\mathcal{I}}(\omega)d\omega \tag{6.7}$$

where $*$ denotes the conjugate complex. Note that $\hat{\mathcal{I}}(\omega) = \hat{\mathcal{I}}^*(-\omega)$ since $\mathcal{P}(t)$ is real.
From this relation, we can define a power transmitted frequency by frequency as

$$\hat{\mathcal{P}}(\omega) = \frac{1}{2\pi}\left(\hat{\mathcal{I}}(\omega) + \hat{\mathcal{I}}^*(-\omega)\right) = \frac{1}{\pi}\mathrm{Re}\left(\hat{\mathcal{I}}(\omega)\right) = \frac{1}{\pi}\int_\Omega \mathrm{Re}\left(\hat{F}^*(x,y,\omega)\cdot i\omega\hat{\Lambda}_p(x,y,\omega)\right)dxdy \tag{6.8}$$

where Re denotes the real part. With the exception of one multiplicative constant, the formula used in [Suzuki, 1986] is the same.

The right-hand-side vector of equation (6.2), which is the force applied to the bridge, is given by

$$\hat{F}(x,y,\omega) = -\chi_\Omega(x,y)\begin{pmatrix}\hat{F}^P\\ \ell\hat{G}^P\\ \ell\hat{H}^P\end{pmatrix} = -\chi_\Omega(x,y)\begin{pmatrix}{}^t\nu_c\\ \ell\,{}^t\tau_c\\ \ell\,{}^t\eta_c\end{pmatrix}\hat{T}_L(w) = -\mathcal{R}_{\alpha\beta}(x,y)\hat{T}_L(\omega) \tag{6.9}$$

where

$$\mathcal{R}_{\alpha\beta} = -\chi_\Omega(x,y)\begin{pmatrix}{}^t\nu_c\\ \ell\,{}^t\tau_c\\ \ell\,{}^t\eta_c\end{pmatrix} \tag{6.10}$$

is the matrix used to characterize the orientation of the string in relation to the soundboard.
The transmitted power is then expressed as a function of admittance

$$\hat{\mathcal{P}}_{\alpha\beta}(\omega) = \frac{1}{\pi}\int_\Omega \mathrm{Re}\left(\hat{\mathbb{Y}}\mathcal{R}_{\alpha\beta}\hat{T}_L\cdot\mathcal{R}_{\alpha\beta}\hat{T}_L\right)dxdy \tag{6.11}$$

At the discrete level, this writes

$$\hat{\mathcal{P}}_{\alpha\beta,h}(\omega) = \frac{1}{\pi}\mathrm{Re}\left(\hat{\mathbb{Y}}_h\mathcal{R}_{\alpha\beta,h}\hat{T}_{Lh}\cdot\mathcal{R}_{\alpha\beta,h}\hat{T}_{Lh}\right) \tag{6.12}$$

with

$$\mathcal{R}_{\alpha\beta,h} = {}^t\mathbb{P}_h^U J_h\,{}^t\nu_{c,h} + \ell\,{}^t\mathbb{P}_h^{\Theta 1}J_h\,{}^t\tau_{c,h} + \ell\,{}^t\mathbb{P}_h^{\Theta 2}J_h\,{}^t\eta_{c,h} \tag{6.13}$$

and where the vectors $\nu_{c,h}$, $\tau_{c,h}$ and $\eta_{c,h}$ depend on the orientations (α,β) via the relation (3.1). This relation (6.12) allows us to observe, frequency by frequency, the influence of the string's lateral β orientation on the power transmitted to the soundboard.

6.3 Transverse impulse response

Let us choose $\hat{T}_L = {}^t(1,0)$ which corresponds to an impulse in the transverse direction of the string. We choose a downbearing angle $\alpha = 4°$ and the impulse is applied on the soundboard at the F_3 string attachment point.
By varying the lateral angle β of the strings (see figure 2), we can draw a power transmission map $\hat{\mathcal{P}}_{\alpha\beta,h}(\omega)$ shown in figure 20.

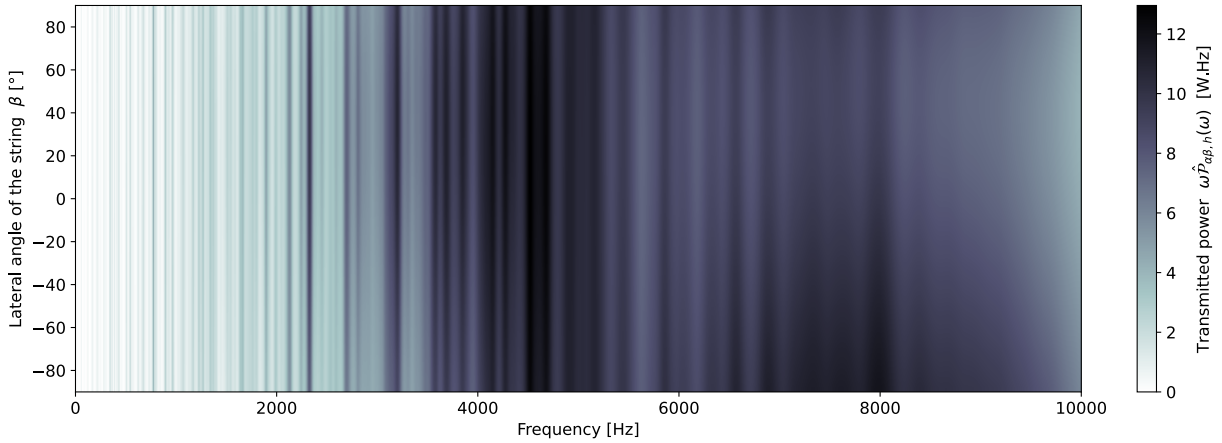

Figure 20: Transmitted power $\omega\hat{\mathcal{P}}_{\alpha\beta,h}(\omega)$ with respect to β (vertical axis) and frequency (horizontal axis).

The quantity plotted on figure 20 is the power multiplied by the pulsation $\omega\hat{\mathcal{P}}_{\alpha\beta,h}(\omega)$ for better visualization. We note that the lateral angle β has very little influence on the power transmission, as shown by the invariance of the color on the vertical axis.

6.4 Longitudinale impulse response

Let's now choose $\hat{T}_L = {}^t(0,1)$ which corresponds to an impulse in the longitudinal direction of the string. We choose a downbearing angle $\alpha = 4°$ and the impulse is applied on the soundboard at the F_3 string attachment point.
By varying the lateral angle of the β strings (see figure 2), we can draw power transmission maps $\hat{\mathcal{P}}_{\alpha\beta,h}(\omega)$ represented on figures 21 and 22.

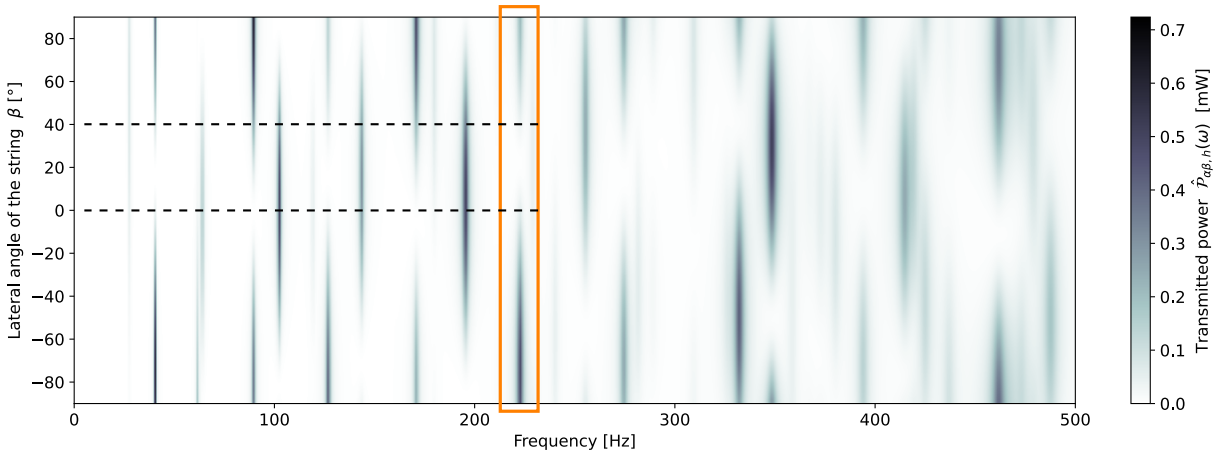

Figure 21: Transmitted power $\hat{\mathcal{P}}_{\alpha\beta,h}(\omega)$ function of β and of frequency [0 - 500 Hz].

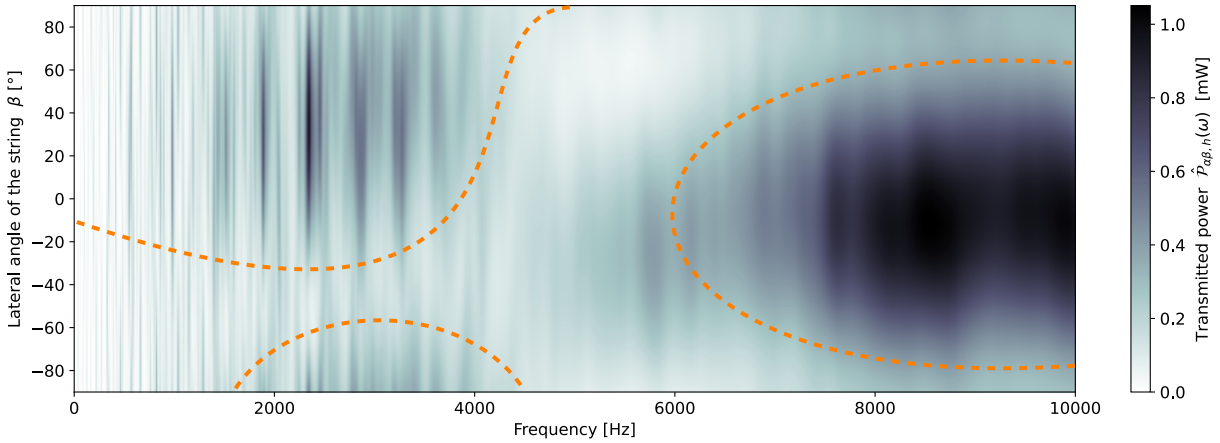

Figure 22: Transmitted power $\hat{\mathcal{P}}_{\alpha\beta,h}(\omega)$ function of β and of frequency [0 - 10 kHz].

On these maps, dark areas correspond to high power transmissions, while light areas correspond to low power transmissions.
Let us take an example of how to read figure 21. Let us imagine that the frequency $f \simeq 222$ Hz (mode 14) framed in orange on the figure is annoying to the ear, too present in the sound, and that a piano maker wishes to attenuate it. In this case, a relevant choice of string orientation would be $\beta \in [0, 40°]$, since, as shown by the very light color of the line for this choice of angle, very little power is transmitted.
However, this possibility is limited by the layout constraints of the piano's various components, which already take a lot of space. Therefore in practice it is not possible to adjust the lateral angle β of each string independently.

If we consider a wider range of frequencies in figure 22, we can see very clearly that darker areas of high power transmission and lighter areas of lower transmitted power form clusters (marked in dotted orange in figure 22). In the mid-frequency range for example, from 1 to 4 kHz, the $\beta > 0$ zone is much darker and transmits much more power than the much lighter $\beta < 0$ zone. In the high-frequency range, from 7 to 10 kHz, an imposing dark spot of high power transmission is visible at angles $\beta \in [-60°, 40°]$.

The transmission map in figure 22 does not reveal any optimal orientations that would uniformly limit or maximize the transmitted power over the entire audible frequency range [20 Hz - 20 kHz]. However, there is a clear difference in behaviour between low and high frequencies. These differences could be explained by the orientations of the wood fibres of the soundboard ($\beta = 54.4°$), stiffeners ($\beta = -40°$) and bridge ($\beta = 23°$), which influence shear strength and could have an influence on power transmission. In fact, it is known that wood strength is higher for torsional forces applied orthogonally to the fibres and, conversely, lower for forces applied parallel to the fibres. To explain the areas of high and low power transmission in figure 22, it would be necessary to be able to assign an importance to the resistance imposed by each element, as a function of frequency.
It's possible, for example, that the wood fibres of the table are small enough to be unnoticeable at low frequencies, but have a significant importance at high frequencies. And vice versa, the stiffeners and bridge, which are quite massive, may have a stronger influence on low frequencies than on high frequencies, or else impose a confinement of vibrations as shown in [Ege, 2009].

We do not go any further into this part, which would require a very detailed study on its own, but we do think it could lead to interesting studies in terms of instrument making.

7 Conclusion and Prospects

In this report, we have developed a bridge model in the form of a coupling condition that allows longitudinal string vibrations to be transmitted to the soundboard.
The numerical method is based on a modal decomposition of the soundboard and an analytical time resolution on a truncated mode sequence. The coupling scheme preserves a discrete energy balance that ensures its stability, and converges quadratically in time.
For realistic string angular configurations (α small), longitudinal waves are well transmitted to the soundboard and precursors are observed.
Finally, the last section studied the soundboard's impulse responses. For an impulse in the transverse direction of the string, we found no significant influence of the lateral β angle on the power transmitted via the bridge. On the other hand, string orientations clearly appear to maximize or minimize the transmission of longitudinal waves over certain frequency ranges. Further studies may enable us to optimize instrument making at this level of the instrument.

Although it allows us to account for the expected physical phenomena, in particular precursors that seem realistic, this model still lacks experimental validation. Experiments would make it possible to validate the use of these coupling conditions as a reduced model of the bridge, or, on the contrary, to envisage more complex modelling, for example by considering the bridge in its entirety as a beam and coupling all its degrees of freedom with those of the soundboard. This problem, typically the coupling of a Timoshenko beam to a Reissner-Mindlin plate, in the time domain and with good energy properties, remains to our knowledge an open problem today.

As mentioned previously in [Chabassier, 2012], our model still does not take into account the downbearing exerted on the soundboard in the resting position. Piano builders are well aware, as we mentioned in the introduction to this report, that adjusting the pressure of the strings on the soundboard at rest is one of the most fundamental criteria for sound quality. A pre-stressed shell model, as in [Mamou-Mani et al., 2008], would perhaps make it possible to better model the transmission of (longitudinal) waves at the bridge. Once again, we lack recent and precise experiments at this level of the instrument to validate or invalidate our models.

Finally, on almost all pianos, the bridges are covered with a layer of graphite that allows the string to slide longitudinally, particularly when tuning, to avoid breaking the bridges. It is therefore possible that the longitudinal waves at the end of the strings are not transmitted entirely to the bridge, but that some of them are also transmitted to the lengths of dead string located after the bridge, which would be interesting to model.

A Modelling and numerical simulation of the strings

This appendix is a condensed extract of [Castera and Chabassier, 2023], in which more detailed explanations about numerical methods for the strings can be found.

A.1 String models

There are many models that can be used to describe strings. Their complexity varies according to the accuracy required and the different physical phenomena taken into account (stiffness, non-linearity, double polarisation). Most of the existing one-dimensional models, with the exception of the Euler-Bernoulli model, can be written in the same unified matrix form.

Model A.1 (Unified matrix formulation of string models)

Seek $q : [0, L] \times [0, T] \longrightarrow \mathbb{R}^N$ so that

$$\begin{cases} \partial_t^2 Mq + \partial_t \left(Rq - \partial_x \left(H \partial_x q\right)\right) \\ \qquad\qquad - \partial_x \left(A\partial_x q + Bq + \nabla \mathcal{U}\left(\partial_x q\right)\right) + Cq + {}^tB\partial_x q = F(x,t) & \text{(A.1a)} \\ \forall k \in \mathcal{I}_D, \forall t \in [0,T], \quad q_k(0,t) = q_k(L,t) = 0 & \text{(A.1b)} \\ \forall k \in \mathcal{I}_N, \forall t \in [0,T], \quad \partial_x q_k(0,t) = \partial_x q_k(L,t) = 0 & \text{(A.1c)} \\ \forall x \in [0,L], \quad q(x,0) = 0 & \text{(A.1d)} \end{cases}$$

where M, A, B, C, R and H are matrices of $\mathcal{M}_N(\mathbb{R})$ and A and C are symmetrical, R and H symmetrical and positives, and M is symmetrical positive-definite. $\mathcal{U} : \mathbb{R}^N \longrightarrow \mathbb{R}$ is the functional that accounts for the nonlinearity.
The sets $\mathcal{I}_D$ and $\mathcal{I}_N$ form a partition of the set $[1, N]$ and determine the boundary conditions (Dirichlet or Neumann) used on the various unknowns.

For the list of models below, we recall the meaning of the physical coefficients. *rho* is the density, S the cross-section, T_0 the tension at rest, E the Young's modulus and G the shear modulus, I the quadratic moment of section, and κ the Timoshenko coefficient.
R_u, R_v, R_φ designate dry damping, and η_u, η_v, η_φ viscous damping.

Vibrating string model (linear non-stiff)

$N = 1$, $q = u_c$, $\mathcal{I}_D = \{1\}$, $\mathcal{I}_N = \emptyset$

$$M = \rho S, \quad A = T_0, \quad R = 2\rho S R_u, \quad H = 2T_0\eta_u, \quad B = C = 0, \quad \mathcal{U} = 0$$

Timoshenko model (linear stiff)

$N = 2$, $q = {}^t(u_c, \varphi_c)$, $\mathcal{I}_D = \{1\}$, $\mathcal{I}_N = \{2\}$

$$M = \begin{pmatrix} \rho S & 0 \\ 0 & \rho I \end{pmatrix}, \quad A = \begin{pmatrix} T_0 + SG\kappa & 0 \\ 0 & EI \end{pmatrix}, \quad B = \begin{pmatrix} 0 & -SG\kappa \\ 0 & 0 \end{pmatrix}, \quad C = \begin{pmatrix} 0 & 0 \\ 0 & SG\kappa \end{pmatrix}$$

$$R = \begin{pmatrix} 2\rho S R_u & 0 \\ 0 & 2\rho I R_\varphi \end{pmatrix}, \quad H = \begin{pmatrix} 2T_0\eta_u & 0 \\ 0 & 2EI\eta_\varphi \end{pmatrix}, \quad \mathcal{U} = 0$$

Geometrically exact model (nonlinear non-stiff)

$N = 2$, $q = {}^t(u_c, v_c)$, $\mathcal{I}_D = \{1, 2\}$, $\mathcal{I}_N = \emptyset$

$$M = \begin{pmatrix} \rho S & 0 \\ 0 & \rho S \end{pmatrix}, \quad A = \begin{pmatrix} T_0 & 0 \\ 0 & ES \end{pmatrix}, \quad R = \begin{pmatrix} 2\rho S R_u & 0 \\ 0 & 2\rho S R_v \end{pmatrix}, \quad H = \begin{pmatrix} 2T_0\eta_u & 0 \\ 0 & 2ES\eta_v \end{pmatrix}$$

$$B = C = 0, \quad \mathcal{U}(u, v) = (ES - T_0)\left[\frac{1}{2}u^2 + (1 + v) - \sqrt{u^2 + (1 + v)^2}\right]$$

Geometrically exact stiff model (nonlinear stiff)

$N = 3$, $q = {}^t(u_c, v_c, \varphi_c)$, $\mathcal{I}_D = \{1, 2\}$, $\mathcal{I}_N = \{3\}$

$$M = \begin{pmatrix} \rho S & 0 & 0 \\ 0 & \rho S & 0 \\ 0 & 0 & \rho I \end{pmatrix}, \quad A = \begin{pmatrix} T_0 + SG\kappa & 0 & 0 \\ 0 & ES & 0 \\ 0 & 0 & EI \end{pmatrix}, \quad B = \begin{pmatrix} 0 & 0 & -SG\kappa \\ 0 & 0 & 0 \\ 0 & 0 & 0 \end{pmatrix}, \quad C = \begin{pmatrix} 0 & 0 & 0 \\ 0 & 0 & 0 \\ 0 & 0 & SG\kappa \end{pmatrix}$$

$$R = \begin{pmatrix} 2\rho S R_u & 0 & 0 \\ 0 & 2\rho S R_v & 0 \\ 0 & 0 & 2\rho I R_\varphi \end{pmatrix}, \quad H = \begin{pmatrix} 2T_0\eta_u & 0 & 0 \\ 0 & 2ES\eta_v & 0 \\ 0 & 0 & 2EI\eta_\varphi \end{pmatrix}$$

$$\mathcal{U}(u, v) = (ES - T_0)\left[\frac{1}{2}u^2 + (1 + v) - \sqrt{u^2 + (1 + v)^2}\right]$$

A.2 Variational formulation and energy

Let us introduce the variational space $\mathcal{Q}_D$ of the functions that cancels at $x = 0$:

$$\mathcal{Q}_D = \left\{ q \in \left(H^1([0, L])\right)^N \;\middle|\; \forall k \in \mathcal{I}_D,\ q_k(0) = 0 \right\} \tag{A.2}$$

The $x = L$ end of the string is not subject to a Dirichlet condition, and we denote T_L the tension exerted there by the external coupling. Seek $q \in \mathcal{Q}_D$ so that for all $q^* \in \mathcal{Q}_D$:

$$\begin{aligned} \int_0^L M\ddot{q} \cdot q^* + \int_0^L R\dot{q} \cdot q^* + \int_0^L H\partial_x\dot{q} \cdot \partial_x q^* \\ + \int_0^L \begin{pmatrix} C & {}^tB \\ B & A \end{pmatrix} \begin{pmatrix} q \\ \partial_x q \end{pmatrix} \cdot \begin{pmatrix} q^* \\ \partial_x q^* \end{pmatrix} + \int_0^L \nabla\mathcal{U}(\partial_x q) \cdot \partial_x q^* \\ = T_L \cdot q^*(L) + \int_0^L F \cdot q^* \end{aligned} \tag{A.3}$$

Theorem A.1 (Power balance of the string model)

Any regular enough solution $q \in \mathscr{C}^1([0, T], \mathcal{Q}_D) \cap \mathscr{C}^2\left([0, T], L^2([0, L])^N\right)$ to the model A.1 verifies

$$\frac{d\mathcal{E}_c}{dt} = T_L \cdot \dot{q}(L, t) + \int_0^L F \cdot \dot{q} - \int_0^L R\dot{q} \cdot \dot{q} - \int_0^L H\partial_x\dot{q} \cdot \partial_x\dot{q} \tag{A.4a}$$

$$\mathcal{E}_c(t) = \frac{1}{2}\int_0^L M\dot{q} \cdot \dot{q} + \frac{1}{2}\int_0^L \begin{pmatrix} C & {}^tB \\ B & A \end{pmatrix} \begin{pmatrix} q \\ \partial_x q \end{pmatrix} \cdot \begin{pmatrix} q \\ \partial_x q \end{pmatrix} + \int_0^L \mathcal{U}(\partial_x q) \tag{A.4b}$$

Proof. Just apply the variational form (A.3) with $q^* = \dot{q} \in \mathcal{Q}_D$. □

Remark A.1

Any regular enough solution $q \in \mathscr{C}^1([0,T],\mathcal{Q}_D) \cap \mathscr{C}^2\left([0,T], L^2([0,L])^N\right)$ *to the model A.1 verifies that*

$$\Big[A\partial_x q + Bq + \nabla\mathcal{U}(\partial_x q) + H\partial_x\dot{q}\Big](x=L,t) = T_L \tag{A.5}$$

A.3 Quadratization with the Scalar Auxiliary Variable method

Let us define a constant $c \in \mathbb{R}_+^*$ such that $2\int_0^L \mathcal{U}(\partial_x q)dx + c$ is strictly positive. We also introduce an auxiliary variable which is independent of the space variable:

$$\forall t \in [0,T], \quad z(t) \equiv \sqrt{2\int_0^L \mathcal{U}(\partial_x q(x,t))dx + c} \tag{A.6}$$

Associated with this auxiliary variable, we define an auxiliary operator G such that

$$G : \left| \begin{array}{ccc} \mathcal{Q}_D & \longrightarrow & L^2([0,L])^N \\ q & \longmapsto & \dfrac{1}{\sqrt{2\int_0^L \mathcal{U}(\partial_x q(x,t))dx + c}}\nabla\mathcal{U}(\partial_x q) \end{array} \right. \tag{A.7}$$

The reformulation of the string equation can be done on the weak formulation. Seek $q \in \mathcal{Q}_D$ et $z \in \mathbb{R}$ so that for all $q^* \in \mathcal{Q}_D$:

$$\begin{cases} \displaystyle\int_0^L M\ddot{q}\cdot q^* + \int_0^L R\dot{q}\cdot q^* + \int_0^L H\partial_x\dot{q}\cdot\partial_x q^* \\ \qquad\qquad + \displaystyle\int_0^L \begin{pmatrix} C & {}^tB \\ B & A \end{pmatrix}\begin{pmatrix} q \\ \partial_x q \end{pmatrix}\cdot\begin{pmatrix} q^* \\ \partial_x q^* \end{pmatrix} + z\int_0^L G(\partial_x q)\cdot\partial_x q^* = \int_0^L F\cdot q^* \end{cases} \tag{A.8a}$$

$$\dot{z} = \int_0^L G(\partial_x q)\cdot\partial_x\dot{q} \tag{A.8b}$$

Since the auxiliary variable z is not distributed, the equation (A.8b) remains a non-variational scalar equation.

Theorem A.2 (Power balance of the SAV formulation)

Any regular enough solution $q \in \mathscr{C}^1([0,T],\mathcal{Q}_D)\cap\mathscr{C}^2\left([0,T], L^2([0,L])^N\right)$ and $z \in \mathscr{C}^1([0,T],\mathbb{R})$ to (A.8) verifies

$$\begin{cases} \dfrac{d\mathcal{E}_c}{dt} = \displaystyle\int_0^L F\cdot\dot{q} - \int_0^L R\dot{q}\cdot\dot{q} - \int_0^L H\partial_x\dot{q}\cdot\partial_x\dot{q} & \text{(A.9a)} \\ \mathcal{E}_c(t) = \dfrac{1}{2}\displaystyle\int_0^L M\dot{q}\cdot\dot{q} + \frac{1}{2}\int_0^L \begin{pmatrix} C & {}^tB \\ B & A \end{pmatrix}\begin{pmatrix} q \\ \partial_x q \end{pmatrix}\cdot\begin{pmatrix} q \\ \partial_x q \end{pmatrix} + \frac{1}{2}z^2(t) & \text{(A.9b)} \end{cases}$$

Proof. Use the weak formulation $q^* = \dot{q} \in \mathcal{Q}_D$. Then equation (A.8b) allows to write that

$$z(t)\int_0^L G(\partial_x q)\cdot\partial_x\dot{q} = z(t)\dot{z}(t) \tag{A.10}$$

□

A.4 Spatial discretization

The spatial discretization is based on high-order spectral finite elements ($r \in \mathbb{N}^*$) on a regular mesh of step Δx such that

$$[0, L] = \bigcup_k [x_k, x_{k+1}] \qquad \text{et} \qquad x_{k+1} = x_k + \Delta x \tag{A.11}$$

The discrete finite element spaces $\mathcal{Q}_h$ and $\mathcal{Z}_h$ have finite dimensions n_h^q and n_h^z respectively and are defined by

$$\begin{aligned} \mathcal{Q}_h &= \left\{ q \in \mathcal{Q}_D \;\middle|\; \forall i \in [\![1, N]\!], \forall k,\ q_{i\,|[x_k, x_{k+1}]} \in \mathbb{P}_r \right\} \\ \mathcal{Z}_h &= \left\{ z \in L^2([0, L]) \;\middle|\; \forall k,\ z_{|[x_k, x_{k+1}]} \in \mathbb{P}_r \right\} \end{aligned} \tag{A.12}$$

and where $\mathbb{P}_r$ is the set of polynomials of degree at most r. The degrees of freedom and quadrature points are chosen like the Gauss-Lobatto points in order to achieve mass lumping. The basis functions of $\mathcal{Q}_h$ are denoted $(\varphi_i)_{i \in [\![1, n_h^q]\!]}$, and those of $\mathcal{Z}_h$ are denoted $(\phi_i)_{i \in [\![1, n_h^z]\!]}$. Finally, we denote Q_h the vector representation of $q_h \in \mathcal{Q}_h$ and Z_h that of $z_h \in \mathcal{Z}_h$ in these respective bases, and we introduce the following matrices and vectors:

$$\begin{cases} \forall (i,j) \in [\![1, n_h^q]\!]^2, \quad (M_h)_{i,j} = \oint_0^L M\varphi_j \cdot \varphi_i & \text{(A.13a)} \\ \forall (i,j) \in [\![1, n_h^q]\!]^2, \quad (R_h)_{i,j} = \oint_0^L R\varphi_j \cdot \varphi_i + \oint_0^L H\partial_x\varphi_j \cdot \partial_x\varphi_i & \text{(A.13b)} \\ \forall (i,j) \in [\![1, n_h^q]\!]^2, \quad (K_h)_{i,j} = \oint_0^L \begin{pmatrix} C & {}^tB \\ B & A \end{pmatrix} \begin{pmatrix} \varphi_j \\ \partial_x\varphi_j \end{pmatrix} \cdot \begin{pmatrix} \varphi_i \\ \partial_x\varphi_i \end{pmatrix} & \text{(A.13c)} \\ \forall (i,j) \in [\![1, n_h^z]\!]^2, \quad (L_h)_{i,j} = \oint_0^L \phi_j \cdot \phi_i & \text{(A.13d)} \\ \forall i \in [\![1, n_h^q]\!], \quad (\mathbb{G}(Q_h))_i = \oint_0^L G(\partial_x q_h) \cdot \partial_x\varphi_i & \text{(A.13e)} \\ \forall i \in [\![1, n_h^q]\!], \quad (F_h)_i = \oint_0^L F \cdot \varphi_i & \text{(A.13f)} \end{cases}$$

where $\oint$ denotes numerical integration by the Gauss-Lobatto quadrature. The auxiliary variable does not require any discretisation in space since it only depends on time. However, we give it the subscript h to indicate that it depends on the approximation in space through its coupling with the unknown q_h.

The semi-discretised formulation in space can then be written in matrix form:

$$\begin{cases} M_h\ddot{Q}_h + R_h\dot{Q}_h + K_hQ_h + z_h\mathbb{G}(Q_h) = F_h & \text{(A.14a)} \\ \dot{z}_h = \mathbb{G}(Q_h) \cdot \dot{Q}_h & \text{(A.14b)} \end{cases}$$

A.5 2-SAV time discretization scheme

The variable Q_h is sampled on a grid $\{t^n = n\Delta t\}$, and the variable z_h on an interleaved grid $\left\{t^{n+1/2} = \left(n + \frac{1}{2}\right)\Delta t\right\}$ inspired by the work of [Ducceschi et al., 2022], [Ducceschi and Bilbao, 2022]. The finite differences discretisation operators are:

$$\mu q^{n+1/2} = \frac{q^{n+1} + q^n}{2}, \quad \delta q^{n+1/2} = \frac{q^{n+1} - q^n}{\Delta t}, \quad \delta\mu q^n = \frac{q^{n+1} - q^{n-1}}{2\Delta t}$$

$$\delta^2 q^n = \frac{q^{n+1} - 2q^n + q^{n-1}}{\Delta t^2}, \quad \{q\}_\theta^n = \theta q^{n+1} + (1 - 2\theta)q^n + \theta q^{n-1}$$

$$\mu z^n = \frac{z^{n+1/2} + z^{n-1/2}}{2}, \quad \delta z^n = \frac{z^{n+1/2} - z^{n-1/2}}{\Delta t}$$

Numerical scheme A.1 (2-SAV scheme)

At each and every iteration, seek $Q_h^{n+1} \in \mathbb{R}^{n_h^q}$ and $z_h^{n+1/2} \in \mathbb{R}$ so that

$$\begin{cases} M_h \delta^2 Q_h^n + R_h \delta\mu Q_h^n + K_h \{Q_h\}_\theta^n + \mu z_h^n \mathbb{G}(Q_h^n) = F_h^n & \text{(A.15a)} \\ \delta z_h^n = \mathbb{G}(Q_h^n) \cdot \delta\mu Q_h^n & \text{(A.15b)} \end{cases}$$

and $Q_h^0 = Q_h^1 = 0$ and $z_h^{1/2} = \sqrt{c}$.

This scheme is linaerly implicit and verifies the following discrete power balance.

Theorem A.3 (Discrete power balance of the 2-SAV scheme A.1)

The solution to the scheme A.1 verifies

$$\begin{cases} \delta \mathcal{E}_c^n = F_h^n \cdot \delta\mu Q_h^n - \|\delta\mu Q_h^n\|_{R_h}^2 & \text{(A.16a)} \\ \mathcal{E}_c^{n+1/2} = \frac{1}{2} \left\|\delta Q_h^{n+1/2}\right\|_{\widetilde{M}_h}^2 + \frac{1}{2} \left\|\mu Q_h^{n+1/2}\right\|_{K_h}^2 + \frac{1}{2} \left(z_h^{n+1/2}\right)^2 & \text{(A.16b)} \end{cases}$$

where $\widetilde{M}_h = M_h + \Delta t^2 \left(\theta - \frac{1}{4}\right) K_h$ is the modified mass matrix.

B $\mathscr{C}^\infty$ source term in space and in time

The following function S is $\mathscr{C}^\infty$ in space and in time

$$S(x,t) = \begin{cases} A\, e^{1-\frac{1}{1-\left(\frac{x-x_0}{\sigma_x}\right)^2}}\, e^{1-\frac{1}{1-\left(\frac{t-t_0}{\sigma_t}\right)^2}} & \text{if} \quad (x,t) \in [x_0-\sigma_x, x_0+\sigma_x] \times [t_0-\sigma_t, t_0+\sigma_t] \\ 0 & \text{else} \end{cases}$$

The source is applied on the space interval $[x_0 - \sigma_x, x_0 + \sigma_x]$ centered in x_0 during a time $2\sigma_t$ on the interval $[t_0 - \sigma_t, t_0 + \sigma_t]$.
A is the chosen amplitude.

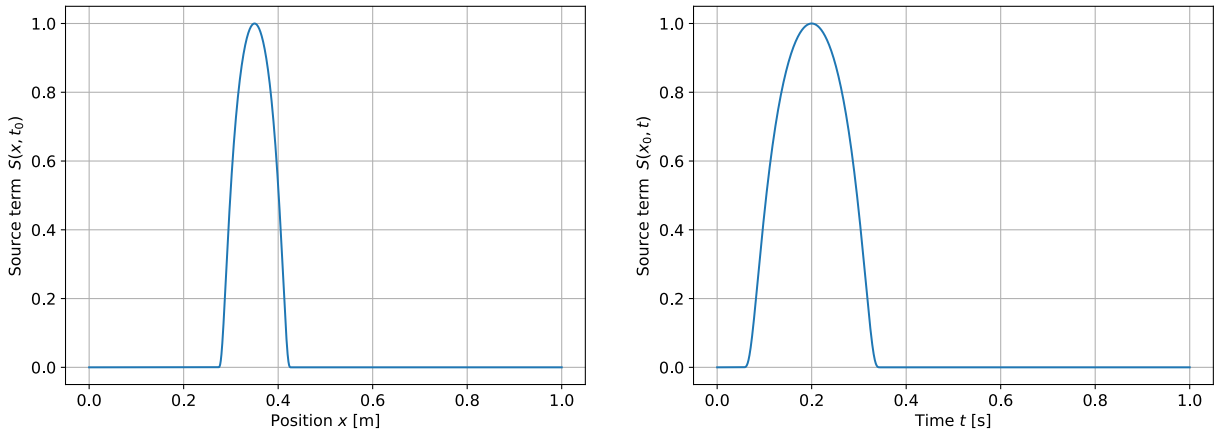

Figure B23: View of the source S for a fixed time (left) and a fixed position (right).

The parameters used to plot the figure B23 are presented in the table B3.

A [-]	x_0 [m]	σ_x [m]	t_0 [s]	σ_t [s]
1	0,35	0,08	0,2	0,15

Table B3: Parameters of the source.

C Exact solution of the soundboard's time scheme

Solving the numerical soundboard scheme is equivalent to solving the following diagonal system of ordinary differential equations with constant second member F for each time step:

$$\begin{cases} \ddot{U}(t) + \mathbb{A}\dot{U}(t) + \mathbb{D}U(t) = F & \text{(C.1a)} \\ U(t_0) = U_0 & \text{(C.1b)} \\ \dot{U}(t_0) = U_1 & \text{(C.1c)} \end{cases}$$

where $\mathbb{A} = \mathrm{diag}(2\alpha_i)$ and $\mathbb{D} = \mathrm{diag}(\lambda_i^2)$

The solution and its time derivative write

$$\begin{cases} U(t) = \mathcal{S}^0_{t-t_0}U_0 + \mathcal{S}^1_{t-t_0}U_1 + \mathcal{R}_{t-t_0}F & \text{(C.2a)} \\ \dot{U}(t) = \dot{\mathcal{S}}^0_{t-t_0}U_0 + \dot{\mathcal{S}}^1_{t-t_0}U_1 + \dot{\mathcal{R}}_{t-t_0}F & \text{(C.2b)} \end{cases}$$

where the diagonal matrices $\mathcal{S}^0$, $\mathcal{S}^1$ and $\mathcal{R}$ are defined by

	If $\lvert\alpha_i\rvert < \lambda_i$	If $\lvert\alpha_i\rvert > \lambda_i$
$(\mathcal{S}^0_t)_{i,i}$	$e^{-\alpha_i t}\left[\cos\left(\tilde{\lambda}_i t\right) + \frac{\alpha_i}{\tilde{\lambda}_i}\sin\left(\tilde{\lambda}_i t\right)\right]$	$e^{-\alpha_i t}\left[\cosh\left(\tilde{\lambda}_i t\right) + \frac{\alpha_i}{\tilde{\lambda}_i}\sinh\left(\tilde{\lambda}_i t\right)\right]$
$(\mathcal{S}^1_t)_{i,i}$	$\frac{1}{\tilde{\lambda}_i}e^{-\alpha_i t}\sin\left(\tilde{\lambda}_i t\right)$	$\frac{1}{\tilde{\lambda}_i}e^{-\alpha_i t}\sinh\left(\tilde{\lambda}_i t\right)$
$(\mathcal{R}_t)_{i,i}$	$\frac{1}{\lambda_i^2}\left(1 - (\mathcal{S}^0_t)_{i,i}\right)$	

and $\tilde{\lambda}_i = \sqrt{|\alpha_i^2 - \lambda_i^2|}$

The proof can be found in [Derveaux, 2002] and in [Chabassier, 2012].

D Generation of the soundboard's listening signals

During the simulations, seismograms of the soundboard are calculated at a list of points (P_i) such that

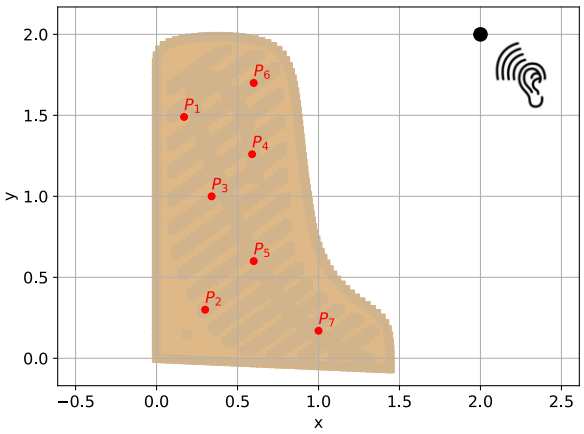

$P_1 = (0.17, 1.49)$ $P_2 = (0.30, 0.30)$
$P_3 = (0.34, 1.00)$ $P_4 = (0.59, 1.26)$
$P_5 = (0.60, 0.60)$ $P_6 = (0.60, 1.70)$
$P_7 = (1.00, 0.17)$

The listening point is located in a realistic position for a listener, at $(2.00, 2.00, 0.60)$, i.e. in the hollow of the grand piano, and 60 centimetres above the soundboard.

To generate the listening signal, we simply sum the soundboard acceleration signals at the points P_i, weighted by the distance d_i separating them from the listening point, and with a corresponding time offset.

$$S(t) = \sum_{i=1}^{7} \frac{1}{d_i} \ddot{u}_p \left(P_i \, , \, t - \frac{d_i}{c} \right) \qquad \left[s^{-2} \right] \tag{D.1}$$

$c = 340$ m/s is the speed of sound in the air surrounding the piano.

References

[Bucur, 2006] Bucur, V. (2006). *Acoustics of wood*. Springer Science & Business Media.

[Castera and Chabassier, 2023] Castera, G. and Chabassier, J. (2023). Numerical analysis of quadratized schemes. Application to the simulation of the nonlinear piano string. Technical Report RR-9516, Inria Bordeaux - Sud-Ouest.

[Chabassier, 2012] Chabassier, J. (2012). *Modélisation et simulation numérique d'un piano par modèles physiques*. PhD thesis, École polytechnique.

[Chaigne and Kergomard, 2008] Chaigne, A. and Kergomard, J. (2008). *Acoustique des instruments de musique*. Belin.

[Conklin, 1996] Conklin, H. A. (1996). Design and tone in the mechanoacoustic piano. part ii. piano structure. *The Journal of the Acoustical Society of America*, 100(2):695–708.

[Corradi et al., 2017] Corradi, R., Miccoli, S., Squicciarini, G., and Fazioli, P. (2017). Modal analysis of a grand piano soundboard at successive manufacturing stages. *Applied Acoustics*, 125:113–127.

[Cuenca and Caussé, 2007] Cuenca, J. and Caussé, R. (2007). Three-dimensional interaction between strings, bridge and soundboard in modern piano's treble range. In *19th international congress on acoustics*, pages MUS–01.

[Derveaux, 2002] Derveaux, G. (2002). *Modélisation numérique de la guitare acoustique.* PhD thesis, Ecole Polytechnique X.

[Ducceschi and Bilbao, 2022] Ducceschi, M. and Bilbao, S. (2022). Simulation of the geometrically exact nonlinear string via energy quadratisation. *Journal of Sound and Vibration*, 534:117021.

[Ducceschi et al., 2022] Ducceschi, M., Bilbao, S., and Webb, C. J. (2022). Real-time simulation of the struck piano string with geometrically exact nonlinearity via a scalar quadratic energy method. In *Proceedings of the 10th European Nonlinear Dynamics Conference*.

[Durufle, 2006] Durufle, M. (2006). *Intégration numérique et éléments finis d'ordre élevé appliqués aux équations de Maxwell en régime harmonique*. PhD thesis, ENSTA ParisTech.

[Ege, 2009] Ege, K. (2009). *La table d'harmonie du piano-Études modales en basses et moyennes fréquences*. PhD thesis, Ecole Polytechnique X.

[Giordano, 1998] Giordano, N. (1998). Sound production by a vibrating piano soundboard: Experiment. *The Journal of the Acoustical Society of America*, 104(3):1648–1653.

[Grob, 2006] Grob, P. (2006). *Méthodes numériques de couplage pour la vibroacoustique instationnaire: éléments finis spectraux d'ordre élevé et potentiels retardés*. PhD thesis, ENSTA ParisTech.

[Mamou-Mani et al., 2008] Mamou-Mani, A., Frelat, J., and Besnainou, C. (2008). Numerical simulation of a piano soundboard under downbearing. *The Journal of the Acoustical Society of America*, 123(4):2401–2406.

[Pfeifle, 2014] Pfeifle, F. (2014). Real-Time Physical Model of a Piano-Hammer String Interaction Coupled to a Soundboard.

[Podlesak and Lee, 1988] Podlesak, M. and Lee, A. R. (1988). Dispersion of waves in piano strings. *The Journal of the Acoustical Society of America*, 83(1):305–317.

[Reblitz, 2005] Reblitz, A. A. (2005). *Le piano: entretien, accord & restauration*. L'Entretemps éd.

[Reissner, 1945] Reissner, E. (1945). The effect of transverse shear deformation on the bending of elastic plates.

[Suzuki, 1986] Suzuki, H. (1986). Vibration and sound radiation of a piano soundboard. *The Journal of the Acoustical Society of America*, 80(6):1573–1582.

[Tan, 2017] Tan, J. J. (2017). *Piano acoustics: string's double polarisation and piano source identification*. PhD thesis, ENSTA ParisTech.

[Valiente et al., 2022] Valiente, P. M., Squicciarini, G., and Thompson, D. (2022). Modeling the interaction between piano strings and the soundboard. In *Fourth Vienna Talk on Music Acoustics*, page 035019, University of Music and Performing Arts, Vienna, Austria.

RESEARCH CENTRE
BORDEAUX – SUD-OUEST

200 avenue de la Vieille Tour

33405 Talence Cedex

Publisher
Inria
Domaine de Voluceau - Rocquencourt
BP 105 - 78153 Le Chesnay Cedex
inria.fr

ISSN 0249-6399